Quarterly Report for

Contract DE-FG36-08GO18192

Stanford Geothermal Program

April-June 2010

Table of Contents

1. FRACTURE CHARACTERIZATION USING PRODUCTION DATA

This research project is being conducted by Research Assistant Egill Juliusson, Senior Research Engineer Kewen Li and Professor Roland Horne. The objective of this project is to investigate ways to characterize fractures in geothermal reservoirs using production data.

1.1 SUMMARY

This report illustrates a new method for the computation of tracer transport through a fracture network, with the inclusion of Taylor dispersion effects. The approach is based on successive convolutions of the one-dimensional advection-dispersion equation, as the tracer travels down the various flow paths between two wells. The computational efficiency of the method was enhanced by performing the convolutions in Laplace space. Special attention was given to the time discretization of in the convolution approach and selection of an algorithm for the numerical inverse Laplace transformation.

The second part of this report ties in with previous investigations on inferring well-to-well connections based on tracer data. In this case we discuss a nonparametric, approach in which the functions are first converted to Laplace space, where the inversion is carried out, and then the resulting estimates are converted back to real space. This method seemed to be infeasible. Finally, a parametric approach to revealing the well-to-well connections is discussed. This approach is based on nonlinear least squares regression, using the trust region reflective algorithm, where the one-dimensional advection-dispersion equation is used as a parametric model function.

1.2 INTRODUCTION

The quarterly report from Fall 2009 discussed a study of tracer and thermal transport through a discrete fracture network using a finite volume reservoir simulator similar to the well known TOUGH2 simulator. The discretization method used allowed explicit simulation of fractures with realistic dimensions. This also enabled us to visualize the propagation of pressure, temperature and tracer saturation in the reservoir with time. The study gave some important insights into the differences between tracer and thermal transport through a fracture network. For example, the tracer response was shown to be more dependent on the specific fracture paths linking two wells than the thermal front. The reason for this was that the (nonreactive) tracer had negligible interaction with the matrix while the thermal front could only propagate when the fracture walls (adjacent matrix elements) had cooled down.

The downside of this full-fledged simulation method was that, the rapid movement of the tracer front in the fractures caused the simulations to be very computational inefficient and numerical dispersion was large and hard to quantify accurately.

In the quarterly report from Winter 2010 a fast but simplified numerical modeling method for calculating flow through a discrete fracture network was discussed. The method was developed based on the assumption of steady-state, incompressible single-phase flow, which made the problem analogous to analyzing a network of resistors. The single-phase

incompressibility assumption should be a relatively good approximation for most EGS (Enhanced Geothermal Systems) and other single-phase geothermal systems.

The way the method works is to take an arbitrary network of fractures and break it down into a set of nodes (fracture intersections) and edges (fracture segments) that connect the nodes. The net inflow into each node is then used to set up a system of equations that describe the flow in the entire network. The system of equations can then be solved to find the flow rate in each fracture segment. At this point, some relatively efficient graph algorithms are employed to find all paths connecting any two wells. The travel time and flow rate attributable to each path can also be found, which means essentially that dispersion free tracer transport through the network has been computed. Being able to solve this problem without any numerical dispersion effects brought us a step closer to characterizing the effects of fracture networks on production data.

In this quarterly report we illustrate how the effects of Taylor dispersion (molecular dispersion within each fracture) can be added to the computations. Our approach is based on successive convolutions of the one-dimensional advection-dispersion equation in Laplace space. Special attention is given to the time discretization in the convolution approach and selection of a numerical algorithm for the inverse Laplace transformation. The results indicate that Taylor dispersion can influence the tracer returns dramatically and mask much of the dispersion caused by the variation of flow paths through the fracture network.

A slightly more involved, but similar, method might be applicable for computation of the thermal response, e.g. based on the analytical solution presented by Gringarten and Witherspoon (1975). The details of how to compute the interaction with the matrix blocks have not been worked out however, and that may prove to be quite challenging.

The quarterly reports from Winter, Spring and Summer 2009 discussed a number of approaches to revealing well-to-well connectivity using tracer data. In this report we present two additional such methods. Each method involves deconvolution; the first is nonparametric and performed in Laplace space; and the second is based on a parametric model. The parametric model used here is based on the solution to the one-dimensional advection-dispersion equation, for a unit impulse injection of tracer

1.3 TAYLOR DISPERSION BY SUCCESSIVE CONVOLUTION IN DISCRETE FRACTURE NETWORKS

The quarterly report in Winter 2010 discussed a simplified way of looking at fracture networks and how to decompose the flow into pulses of tracer coming through each flow path between two wells. The outcome was a way to visualize the dispersion attributable to the complexity of the fracture network, without any interference from numerical dispersion. An example with four wells is shown in Figure 1.1. The wells are depicted with red lines.

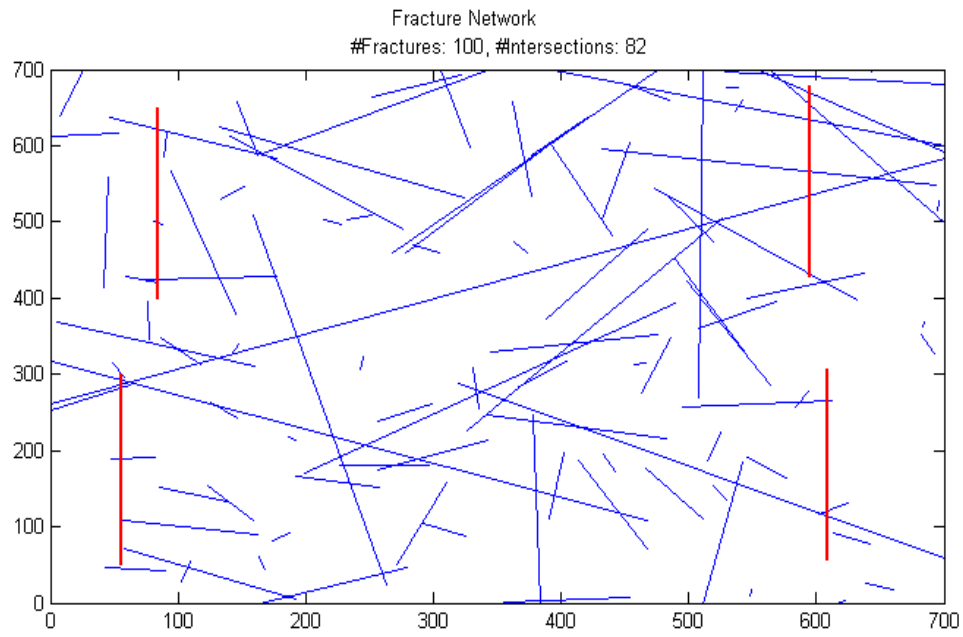

Figure 1.1: An example fracture network with two injection wells (red lines to the left) and two production wells (red lines to the right).

The pressure in the two wells to the left (the injectors) was set to 200 bar while the right most wells (the producers) had a constant pressure of 198 bar. The network was then simplified and the flow through it was computed via nodal analysis. The flow directions are shown in Figure 1.2.

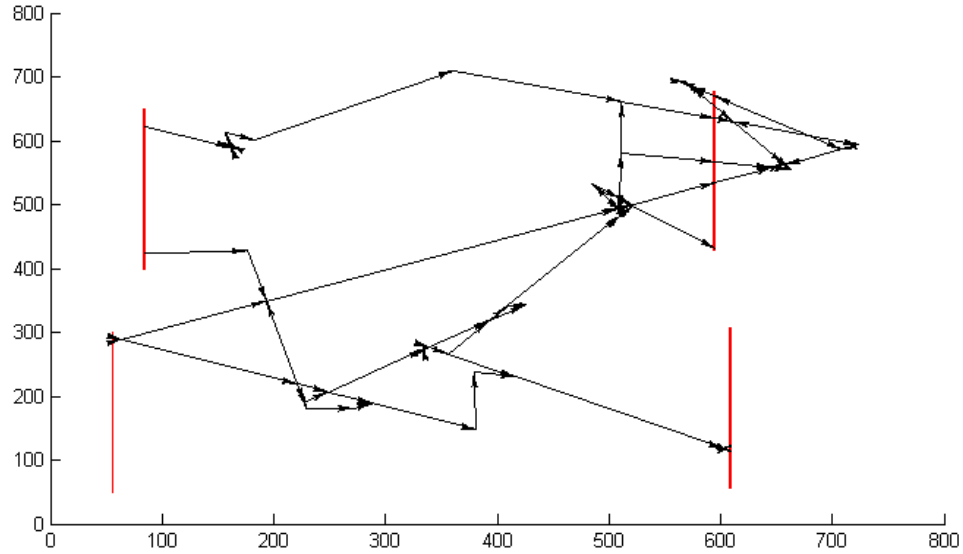

Figure 1.2: Flow paths and directions of flow through the fracture network presented in Figure 1.1.

The dispersion attributable to the fracture network can be generated by collecting the arrival time and flow amount along each path. This is shown in Figure 1.3 (top) along with the cumulative amount of flow recovered (bottom).

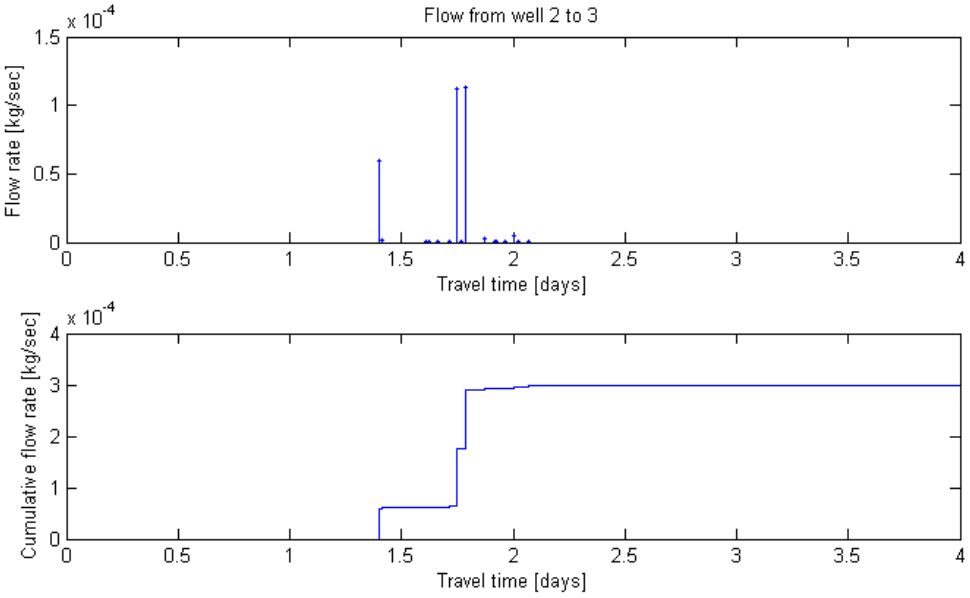

Figure 1.3: These plots illustrate the arrival time versus the amount of flow travelling along each path from well 2 (upper left) to well 3 (upper right).

Note that from these graphs we can see that three flow paths transmit the bulk of the flow from well 2 to well 3. Figure 1.4 illustrates the paths and labels the largest (in terms of flow), the most transmissible and the fastest.

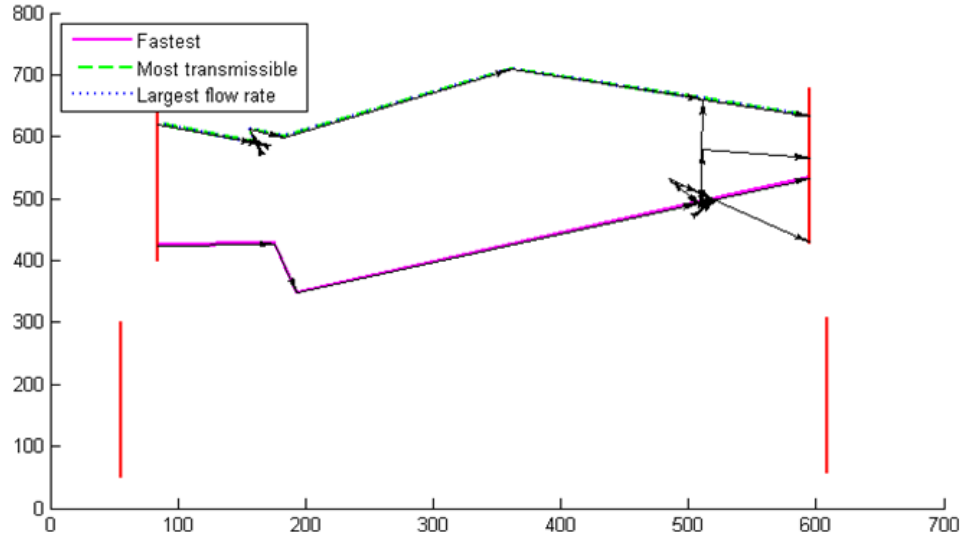

Figure 1.4: Flow paths from well 2 to well 3. Note that the fastest flow path is different from the most transmissible and largest flow path.

All but fracture-induced dispersion effects (most importantly numerical dispersion) are circumvented in these calculations. That also means that some physically realistic dispersion effects need to be added, such as Taylor dispersion (Horne and Rodriguez, 1983), which is a significant effect generated by the interplay between molecular diffusion and the development of a velocity profile between two parallel plates. It is important to understand the relative contribution of this effect as compared to the dispersion effects induced by the multiple flow paths through the fracture network to be able to understand whether it is plausible to extract information about individual fractures (or fracture paths) explicitly from tracer data. As discussed in the quarterly report from Fall 2009, this type of comparison is not easily done using traditional finite volume reservoir models because of numerical dispersion effects.

An analytical solution to the one-dimensional advection-dispersion equation was used to compute the Taylor dispersion effects. The unit impulse kernel for this equation is defined as

$$\begin{aligned}\kappa(t) &= \frac{u}{\sqrt{4\pi Dt}}\exp\left[-\frac{(L-ut)^2}{4Dt}\right] \\ &= \frac{1}{\sqrt{4\pi t_d t}}\exp\left[-\frac{(t_a-t)^2}{4t_d t}\right]\end{aligned} \tag{1.1}$$

where L is the length of the fracture segment, u is the flow velocity and D is the dispersion coefficient. The time values t_a and t_d are the advective and dispersive time scales, defined as

$$t_a = L/u \tag{1.2}$$

and

$$t_d = D/u^2 \tag{1.3}$$

If a tracer slug of concentration c_o released at location $x=0$ over a (small) time interval Δt, the response seen at distance L_1 would be as described by following the convolution equation:

$$c_1(L_1,t) = \int_0^t c_o \Delta t \delta(t-\tau)\kappa_1(\tau)d\tau = \frac{c_o \Delta t u_1}{2\sqrt{\pi D_1 t}}\exp\left[-\frac{(L_1-u_1 t)^2}{4D_1 t}\right] \tag{1.4}.$$

Here the subscript *1* refers to the properties of fracture segment 1 (edge 1, linking nodes 1 and 2). Similarly, the response at the next node (node 3, which we assume to be linked to node 2 via edge 2) could be computed by the convolution of $c_1(t)$ and the unit impulse kernel for edge 2.

$$c_2(L_2,t) = \int_0^t c_1(L_1, t-\tau)\kappa_2(\tau)d\tau \tag{1.5}$$

Considering the fact that node 2 could branch out to more than one edge (say edges 3 and 4) the response at node 3 could be computed as

$$c_2(L_2,t) = \frac{q_2}{q_2+q_3+q_4}\int_0^t c_1(L_1, t-\tau)\kappa_2(\tau)d\tau \tag{1.6}$$

Continuing in this manner all the way to the final node gives the effective dispersive response along each path. Taylor dispersion was modeled by using Equation (1.7) to compute the dispersion coefficient in each fracture segment (Horne and Rodriguez 1983).

$$D_{Taylor} \approx \frac{2}{105}\frac{u^2 b^2}{D_{mol}} \tag{1.7}$$

The molecular diffusion coefficient, D_{mol}, was set to 10^{-10} m^2/s.

In general, the response for each path, K, was computed as

$$c_K(t) = c_o \Delta t q_{tot} \prod_k \frac{q_k}{\sum_l q_l} \coprod_k \kappa_k(t) \tag{1.8}$$

where k runs over all edges on path K, and l runs over all edges with outflow from the node which edge k has flow out of. The symbol $\coprod$ denotes the successive convolution of all the kernels on path K.

In performing these successive convolutions numerically one must pay special attention to the time discretization used for the kernels. The operation can be viewed as generating two vectors, κ_1 and κ_2, with equal time discretization and taking the inner product between the first and the second, by incrementally shifting the second and padding non-overlapping parts with zeros. This is better illustrated by the following example. Suppose:

$\kappa_1 = [\ 1\ \ 2\ \ 3];\quad \kappa_2 = [0\ \ -1\ \ 4]$

Then the convolution of the two would be computed by the taking the following inner products:

```
        1  2  3
4  –1   0                  →                  0

        1  2  3
```

```
4 -1  0                  →          -1

   1  2  3
   4 –1  0               →           2

   1  2  3
      4 –1  0            →           5

   1  2  3
         4 –1  0         →          12
```

Note that here it is implied that the discretization interval is $d\tau=1$ and more importantly it must be the same for each κ such that the inner products make sense in view of them approximating the convolution integral. This method is relatively quick and simple when convolving only a few vectors with relatively few values. The outcome of convolving two vectors of size n and m will be of size $n+m-1$. Therefore, the length of one of the vectors used for each successive convolution will increase rapidly making this method computationally inefficient. Note that the size of $d\tau$ would often be quite small since it must be small enough to capture the sharp peaks in some of the kernel functions. This in turn made the length of the κ vectors large.

Successive convolutions are more easily dealt with in Laplace space, since convolution turns into multiplication under the Laplace transform. Taking the Laplace transform of Equation (1.8) gives:

$$\begin{aligned} L[c_K(t)] &= L[c_o \Delta t q_{tot} \prod_k \frac{q_k}{\sum_l q_l} \coprod_k \kappa_k(t)] \\ &= c_o \Delta t q_{tot} \prod_k \frac{q_k}{\sum_l q_l} L[\coprod_k \kappa_k(t)] \\ &= c_o \Delta t q_{tot} \prod_k \frac{q_k}{\sum_l q_l} \prod_k \tilde{\kappa}_k(s) \end{aligned} \tag{1.9}$$

The Laplace transform of the kernel function for the one-dimensional advection-dispersion equation is:

$$\begin{aligned} \tilde{\kappa}_k(s) &= \frac{u_k}{\sqrt{4D_k s + u_k^2}} \exp\left[\frac{u_k - \sqrt{4D_k s + u_k^2}}{2D_k} L_k \right] \\ &= \frac{1}{\sqrt{4t_{d,k} s + 1}} \exp\left[\frac{t_{a,k}\left(1 - \sqrt{4t_{d,k} s + 1}\right)}{2t_{d,k}} \right] \end{aligned} \tag{1.10}$$

Given this form of $\tilde{\kappa}_k(s)$ in Laplace space the path kernel can quickly be computed as:

$$\tilde{\kappa}_K(s) = \prod_k \tilde{\kappa}_k(s) \tag{1.11}$$

And then $\tilde{\kappa}_K(s)$ can be numerically transformed back to the time domain at well chosen time values, using a suitable numerical inversion method.

We tried working with two numerical inversion methods, the Stehfest method (Stehfest, 1970) and the Den Iseger method (Den Iseger, 2005). Both methods computed function values in real space, at user-supplied time values, given the functional form in Laplace space. The Stehfest algorithm was advantageous in the fact that it worked with any set of time values, while the Den Iseger algorithm was designed to return values at evenly spaced time intervals. Both algorithms were relatively easy to implement, although the Den Iseger method did require complex number arithmetic. The Stehfest algorithm ran faster, but was less accurate, especially when it came to inverting functions that have a lot of variability at late times. That is, in cases where sharp responses at late times needed to be inverted, the Stehfest algorithm would fail while the Den Iseger method worked seamlessly, as illustrated in Figure 1.5.

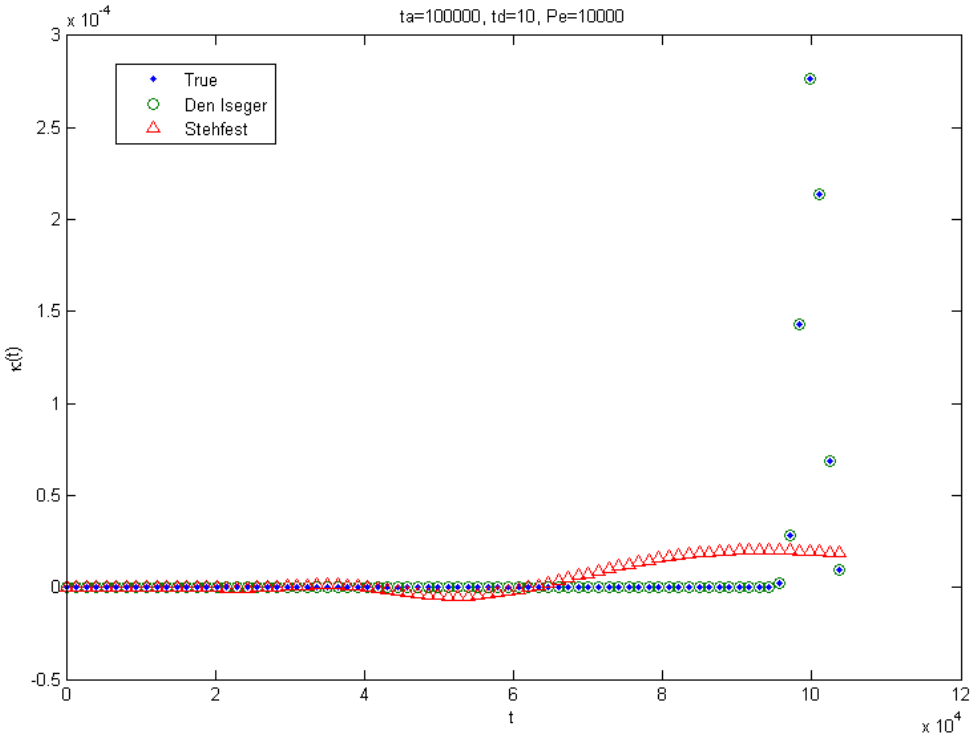

Figure 1.5: Inverting kernels with high Peclet numbers worked well with the Den Iseger method while the Stehfest algorithm would fail.

Another important part of being able to invert the tracer kernels successfully was to make sure that an appropriate time discretization was selected. The kernels could take on various shapes as shown in Figure 1.6

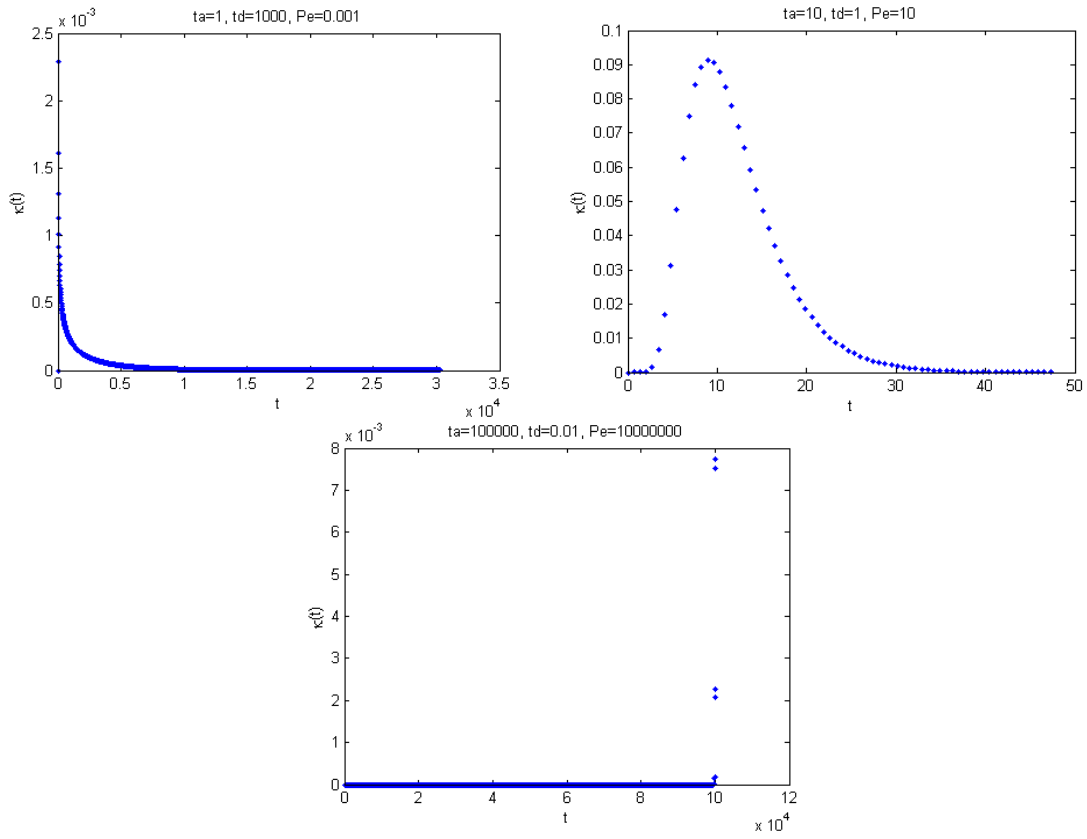

Figure 1.6: Kernels with Peclet numbers 10^{-3} (top left), 10 (top right) and 10^{7} (bottom).

In general, the kernels with low Peclet numbers ($uL/D = t_a/t_d$) have a sharp peak at early times and kernels with high Peclet numbers have a sharp peak at late times. To be able to capture these peaks properly with an even time discretization, we had to make sure that the time interval used was sufficiently fine. To make this possible we computed the time location of the peak, t_{peak}, and the time at which the integral of the kernel reaches a certain small fraction, $t_{take\ off}$.:

$$t_{peak} = \sqrt{t_a^2 + t_d^2} - t_d \tag{1.12}$$

$$t_{take off} \approx 2t_d erfc^{-1}(2\varepsilon) - 2\sqrt{t_d^2\left(erfc^{-1}(2\varepsilon)\right)^2 + t_a t_d erfc^{-1}(2\varepsilon)} + t_a \tag{1.13}$$

where, ε, is a small faction of one, e.g. 10^{-3}. These time values bracket the transient part of the rise in concentration of the tracer slug. We decided that ten numerical values should suffice to capture this transient and thus chose the discretization time interval:

$$dt = \frac{t_{peak} - t_{take\ off}}{10} \tag{1.14}$$

Then, to determine the final value in the discretization we used an approximation similar to Equation (1.13), that is:

$$t_{final} \approx 2t_d erfc^{-1}(2\sqrt{1-\varepsilon}) + 2\sqrt{t_d^2\left(erfc^{-1}(2\sqrt{1-\varepsilon})\right)^2 + t_a t_d erfc^{-1}(2\sqrt{1-\varepsilon})} + t_a \tag{1.15}$$

So the final discretization would be from *0* to t_{final} with spacing *dt*, but to remain practical in the computational effort we capped the number of discretization values at 2000 points.

The inversion and discretization were tested for a wide range of t_a and t_d values. One of the most meaningful ways of testing the quality of the results was to evaluate the integral of the kernels numerically, as this integral should equal 1. It turned out that results of identical quality were obtained as long as the ratio t_a/t_d remained the same. This ratio is the Peclet number. Figure 1.5 shows the integral of the kernel function versus the Peclet number for the kernel, with the kernel computed from the true equation in real space, and inverted from Laplace space using the Den Iseger and the Stehfest method. Because the discretization was finite, there were some errors in then numerical integration even when the true equation was used. This was most evident for Peclet numbers less than 1 and more than 10^7, but that error could be reduced by allowing the number of discretization points to exceed 2000. Moreover, it was clear that the Den Iseger method was very accurate for the entire range of values tested and the quality of the kernels computed by the Den Iseger method were entirely controlled by the quality of the time discretization. The Stehfest method, on the other hand, would only work for Peclet numbers less than or equal to 10. This is why the Den Iseger method was the preferred candidate for inverting the successive convolutions back to real space.

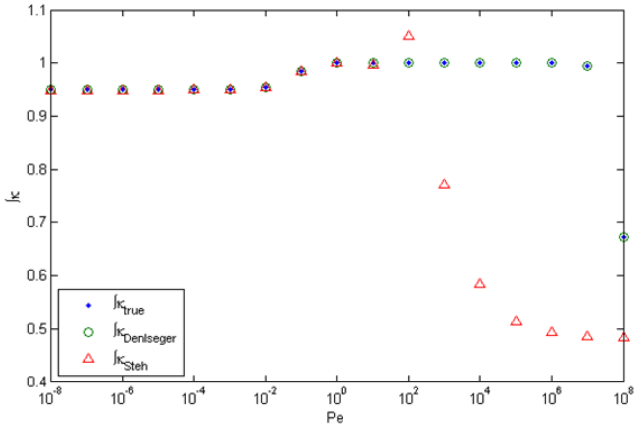

Figure 1.7: A comparison of the numerical integral of the discrete kernel function as computed analytically in real space (true) or analytically in Laplace space and then inverted to real space by the Den Iseger method or the Stehfest method. The comparison is made over a range of Peclet numbers. The ideal result should always equal one.

The construction of the time discretization discussed in Equations (1.12) to (1.15) was based only on a single kernel. When dealing with the inversion of a kernel composed of successive convolutions, the time discretization was modified such that, in stead of taking *dt* as described in (1.14), we used:

$$dt_K = \frac{\sum_k t_{peak} - \sum_k t_{take\ off}}{10} \tag{1.16}$$

where k goes over all the edges (fracture segments) on path K. Then:

$$t_{final,K} = \sum_k t_{final,k} \tag{1.17}$$

The justification for this is that each kernel can be viewed as a probability distribution for a random number, say X_k. The successive convolution of those distributions is equivalent to finding the probability distribution for the sum $Y=\Sigma_k X_k$. This means that the extreme values (analogous to $t_{take\ off}$ and t_{final}) should sum up to even more extreme values for *Y*. For skewed distributions, the individual peak values will not sum up to the peak of the combined distribution, but this effect did not seem to matter much for the numerous cases we tested.

By solving the problem of successive convolutions we were able to compute and compare the effects of Taylor dispersion to the effects of fracture induced dispersion on tracer returns. Figure 1.8 (top) shows the tracer return from well 2 flowing to well 3 if Taylor dispersion is included. The lower part of the figure shows the returns coming from individual flow paths. These return profiles indicate that at least two of the three main flow paths could be identified. Note that these computations were based on the same scenario as in Figure 1.4.

The cumulative returns were compared to the cumulative returns computed without dispersion, as shown in Figure 1.9.

Figure 1.9 shows that in this case the fracture-induced dispersion is significant and thereby one might hope to gain some information about the properties of the more significant flow paths between the wells. On the other hand, this result was very sensitive to the way the relationship between fracture length, *L*, and aperture, *b*, was defined. Models of the type $b=aL^s$ are referred to in the literature (Watanabe and Takahashi, 1995), where *a* and *s* are constants. For the case presented in Figures 1.2-1.4 and 1.8-1.9 we used:

$$b = 1.5\times10^{-5} L^{0.6} \tag{1.18}$$

The fracture lengths were drawn from a lognormal distribution and therefore *b* was also distributed log-normally with values ranging from about 0.1 to 1 mm (Figure 1.10).

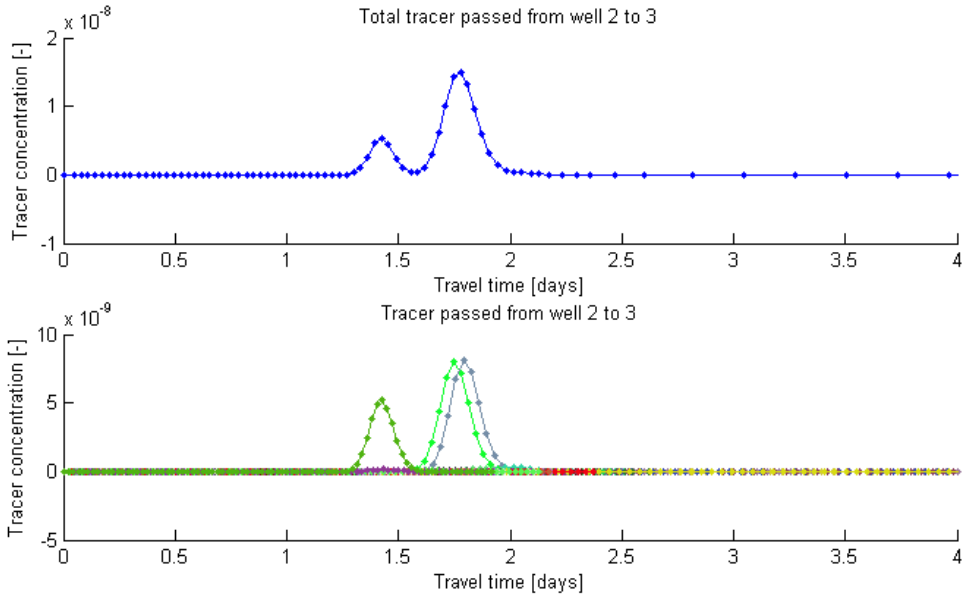

Figure 1.8: Tracer return curves of tracer from well 2 to well 3 including Taylor dispersion. The top plot has the total tracer return, while the lower plot shows the returns coming from each individual path. The largest slugs have a relatively high Peclet number, i.e. little dispersion.

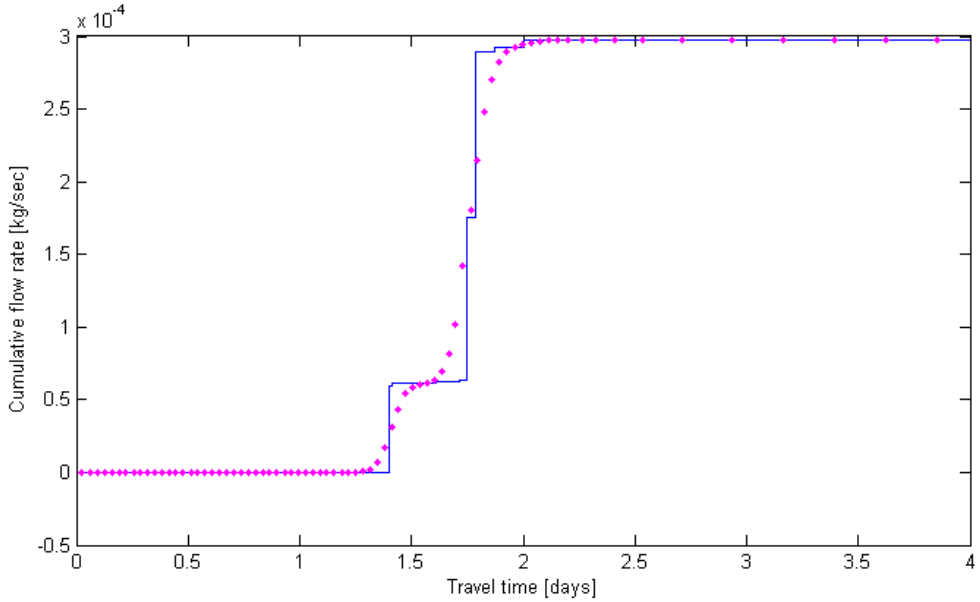

Figure 1.9: A comparison of the cumulative tracer returns (assuming 100% tracer injection) with (magenta dots) and without (blue line) Taylor dispersion. It seems fair to say that that the fracture induced dispersion is significant in this case, since it clearly affects the shape of the return curve.

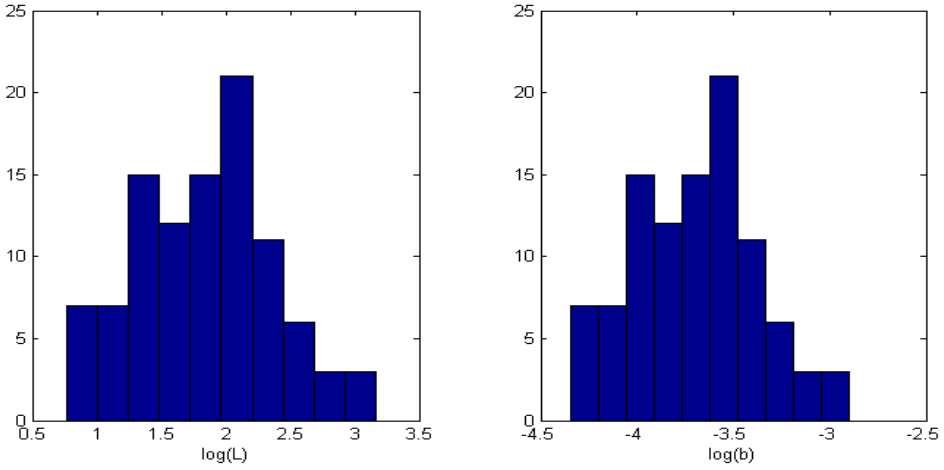

Figure 1.10: Distribution of the log of fracture lengths and aperture values.

Then we tried a slight change in way the apertures were modeled, by taking:

$$b = 3\times10^{-5} L^{0.6} \tag{1.19}$$

Now the apertures ranged from approximately 0.2 to 2 mm. A computation of the tracer returns for the same scenario as referred to in Figures 1.8 and 1.9 gave the results seen in Figures 1.11 and 1.12.

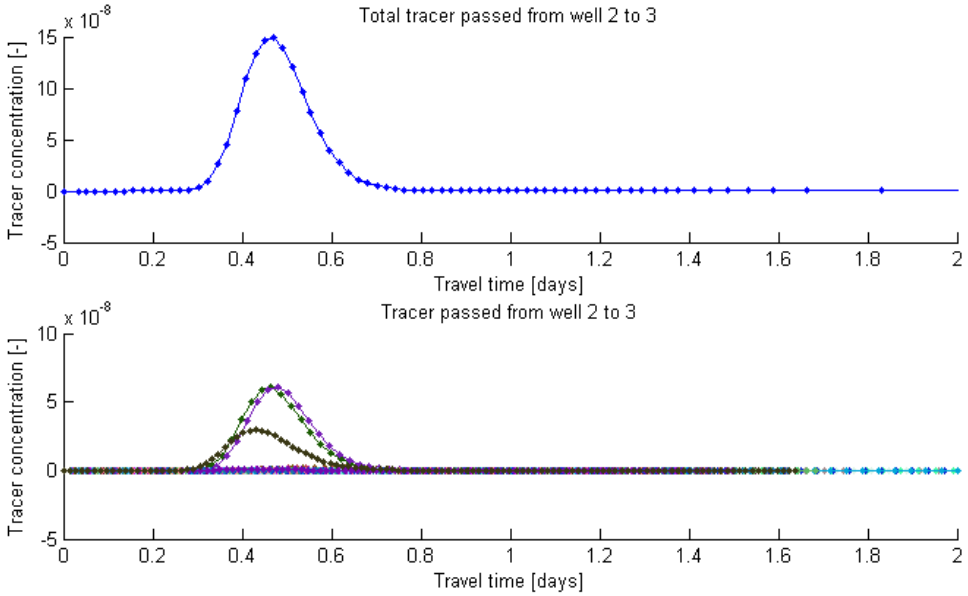

Figure 1.11: Tracer return curves of tracer from well 2 to well 3 including Taylor dispersion. The top plot has the total tracer return, while the lower plot shows the returns coming from each individual path. The largest slugs have a relatively low Peclet number, i.e. high dispersion.

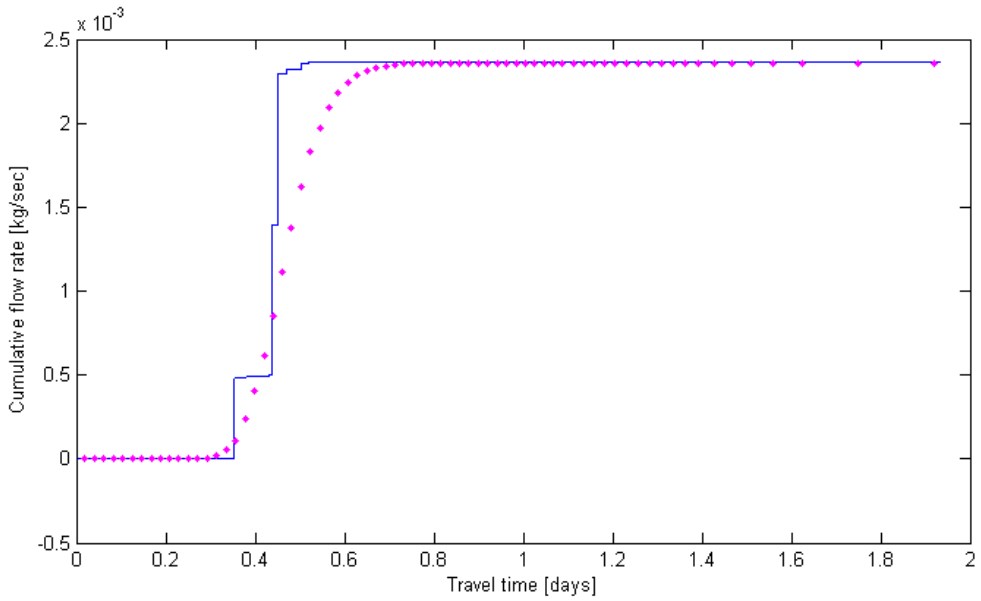

Figure 1.12: A comparison of the cumulative tracer returns (assuming 100% tracer injection) with and without Taylor dispersion. Here Taylor dispersion has become large enough to mask the contribution from individual fractures.

Note that the seemingly small change in the way the fracture apertures were modeled had a significant effect on the tracer returns. The three flow paths were now indistinguishable, because of the Taylor dispersion, which was in turn proportional to the square of the aperture. In other words, large apertures caused the low Peclet numbers, which made it harder to identify individual flow paths from tracer returns. From the definitions of Taylor dispersion and the Peclet number:

$$Pe = \frac{uL}{D_{Taylor}} = \frac{uL}{\frac{2}{105}\frac{u^2b^2}{D_{mol}}} = \frac{105}{2}\frac{D_{mol}L}{b^2}\frac{Hb}{q} \tag{1.20}$$

This shows that the Peclet number was approximately proportional to the inverse of the aperture and the inverse of the flow rate (and $q \sim k \sim b^2$). This meant the tracer returns from the largest flow paths would tend to have the lowest Peclet numbers (i.e. be most dispersed), and therefore these would tend to mask the returns coming from smaller flow paths. This effect is unfortunate since it could eliminate the possibility of identifying the number of dominant flow paths between two wells. It is important to understand that this is may well be a common phenomenon, and that should be kept in mind in the interpretation of tracer tests.

1.4 INFERRING WELL-TO-WELL CONNECTIVITY

The quarterly reports from Winter, Spring and Summer 2009 discussed a number of ways to infer well-to-well connectivity based on tracer data. A simple yet effective way was to

compute the correlation between the time-shifted injection histories and the production history. A similar approach with time-shifted injection histories was used in conjunction with the ACE algorithm to find the optimal, smooth, transformations between the injection and production data. The strength of the ACE algorithm is it quantifies the variability in the production data due to each injection data series, without a predefined relationship between the two. A slightly more restrictive approach to the problem was taken by using a nonparametric deconvolution technique to quantify the transfer function (i.e. tracer kernel) between well pairs. This technique does not require a specific functional form for the kernel, other than it must have some degree of smoothness. The main restriction is that the data used to solve the problem must be obtained at steady-state flow conditions, with only the tracer concentration varying. This is perhaps both the strength and weakness of this approach. The strength is that the well-to-well connections are specific to a specific combination of input flow rates, and therefore the input flow rates could be varied until an optimal set of connections is found. The main weakness is that obtaining enough data to find the connections at each set of input flow rates may take several months or years.

In this section we discuss two additional deconvolution methods for inferring well-to-well connectivity. The first did not turn out to be useful but is documented for completeness. It is based on a nonparametric deconvolution approach where the problem is transferred to Laplace space to investigate the possibility of using a regularization constraint derived from the functional form of the tracer kernel in Laplace space. The second method was quite restrictive, in that a specific functional form for the kernel was assumed, and we invert to find the parameters controlling that functional form.

1.4.1 Nonparametric deconvolution in Laplace space

The general multi-well tracer deconvolution problem is to find the kernel functions, $\kappa_k(t)$, for each producer-injector pair, by solving the equation:

$$c_p(t) = \sum_{k=1}^{N_r} \int_0^t c_{r,k}(t-\tau)\kappa_k(\tau)d\tau \tag{1.21}$$

where c_p is the produced tracer concentration, c_r is the injected tracer concentration and N_r is the number of injectors. In the nonparametric deconvolution approach, we treat $\kappa_k(t)$ as unknown at each time, t. Thus, when there are more than one injector this problem is underdetermined and some sort of regularization must be applied to obtain a degree of continuity in the estimate for $\kappa_k(t)$. Such methods were also discussed in the quarterly report from Summer 2009. Although those methods worked reasonably well, the kernel estimates would tend to show unrealistic fluctuations at late times, where the true solution would tend monotonically to zero.

Equation (1.21) can be converted to Laplace space, to yield:

$$\tilde{c}_p(s) = \sum_{k=1}^{N_r} \tilde{c}_{r,k}(s)\tilde{\kappa}_k(s) \tag{1.22}.$$

where s is the Laplace time variable and the tilde overbars denote the Laplace transforms of the corresponding functions in real space. Equation (1.22) shows more clearly how underdetermined the problem is, i.e. there are N_r unknown variables for each equation. Therefore, a regularization could be applied to find a meaningful solution for $\tilde{\kappa}_k(s)$. The regularization method that we had in mind involved a utilization of the fact that; the one-dimensional kernel function in Laplace space is negative and monotonically increasing for all odd derivatives (with respect to s), and positive and monotonically decreasing for all even derivatives. Or more succinctly:

$$\tilde{\kappa}_k(s) = \frac{1}{\sqrt{4t_{d,k}s+1}} \exp\left[\frac{t_{a,k}\left(1-\sqrt{4t_{d,k}s+1}\right)}{2t_{d,k}}\right] \tag{1.23}$$

and:

$$\begin{aligned} \frac{\partial^{2n+1}\tilde{\kappa}_k(s)}{\partial s^{2n+1}} &\le 0, \quad n \in \{0,1,2,...\} \\ \frac{\partial^{2n}\tilde{\kappa}_k(s)}{\partial s^{2n}} &\ge 0, \quad n \in \{0,1,2,...\} \end{aligned} \tag{1.24}$$

For Equation (1.24) we assumed that s was real valued (as opposed to complex). This meant that the outcome of our estimations should belong to a family of infinitely smooth functions, in the sense that it should have smooth derivatives of all orders.

To test whether this regularization condition was unique enough to allow reasonable kernel estimates in real space we created orthogonal injection histories of the type:

$$c_{r,k}(t) = \sum_{j=1}^{N_{ch}} a_{j,k} H(t - t_{j,k}) \tag{1.25}$$

where N_{ch} is the number of changes in injection, H is the Heaviside step function, $a_{j,k}$ is a multiplier defining the injection amount and $t_{j,k}$ is the time at which the injections change. In Laplace space:

$$\tilde{c}_{r,k}(s) = \sum_{j=1}^{N_{ch}} \frac{a_{j,k} \exp(-t_{j,k}s)}{s} \tag{1.26}.$$

The production history in Laplace space could be computed from Equations (1.22), (1.23) and (1.26).

$$\tilde{c}_p(s) = \sum_{k=1}^{N_r} \sum_{j=1}^{N_{ch}} \frac{a_{j,k} \exp(-t_{j,k}s)}{s\sqrt{4t_{d,k}s+1}} \exp\left[\frac{t_{a,k}\left(1-\sqrt{4t_{d,k}s+1}\right)}{2t_{d,k}}\right] \tag{1.27}.$$

Figure 1.13 shows the injection histories for two wells, two randomly chosen kernels that define the connection to a production well, and the corresponding production history computed by Equation (1.21).

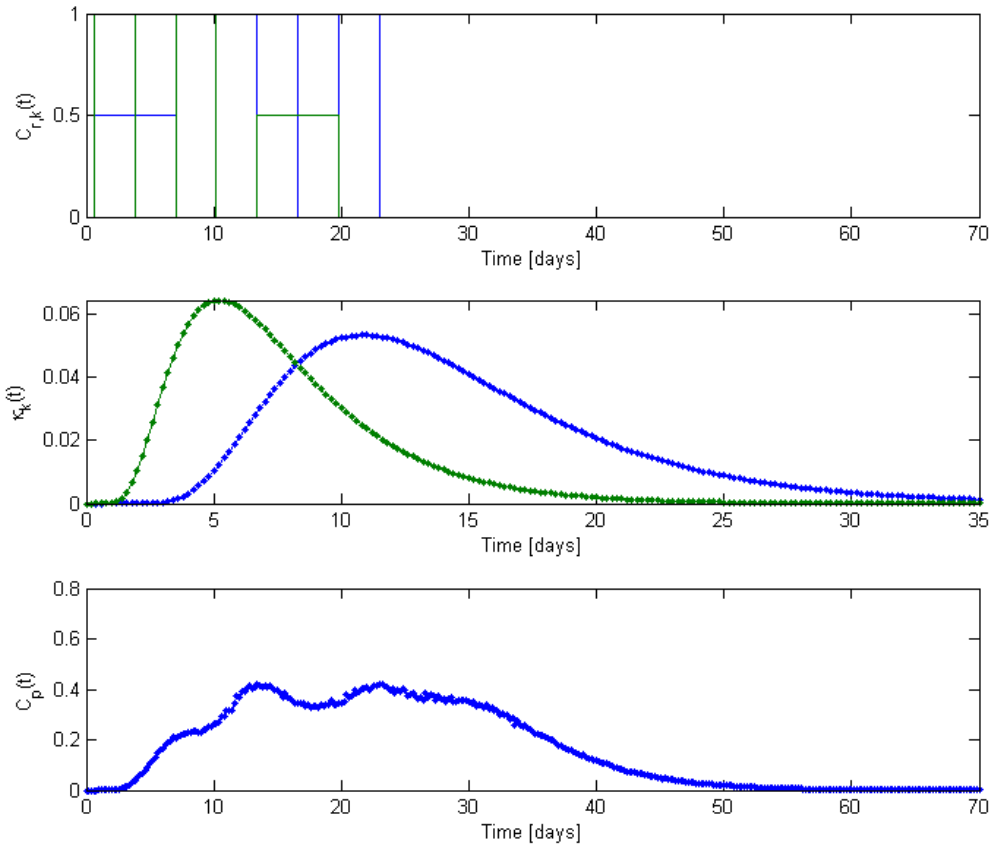

Figure 1.13: Injection histories for two wells (top) and the corresponding tracer kernels (middle) defining the connection to a production well with the production history shown on the bottom plot.

The corresponding functions in Laplace space are illustrated in Figure 1.14.

Before figuring out the details of how to solve Equation (1.22) subject to the constraints defined by Equation (1.24), we tried solving it without regularization in a least squares sense. This is the pseudoinverse solution, i.e.

$$\vec{\kappa}(s_i) = \begin{bmatrix} \kappa_1(s_i) \\ \kappa_2(s_i) \\ \vdots \\ \kappa_{N_r}(s_i) \end{bmatrix} = \left(\vec{c}_r(s_i) \vec{c}_r(s_i)^T \right)^{-1} \vec{c}_r(s_i) c_p(s_i) \tag{1.28}$$

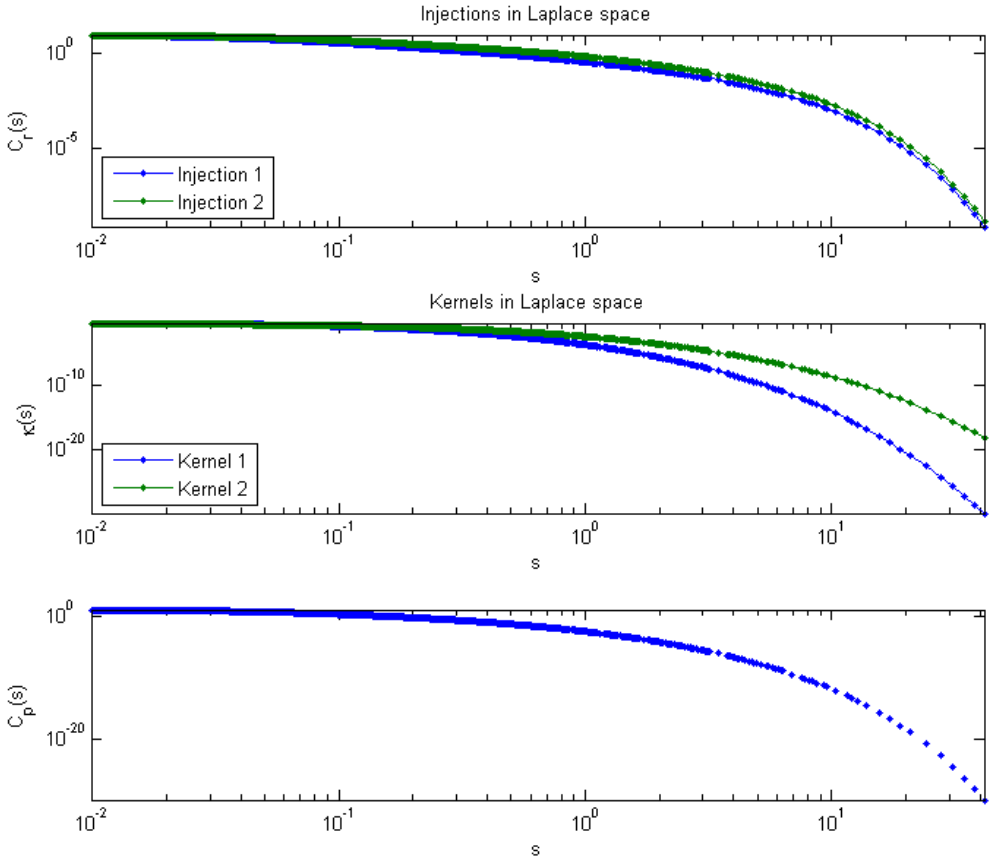

Figure 1.14: Laplace space version of injection histories for two wells (top) and the corresponding tracer kernels (middle) defining the connection to a production well with the production history shown on the bottom plot

With this solution we were able to find kernel estimates that reproduced the production data exactly, as illustrated in Figure 1.15.

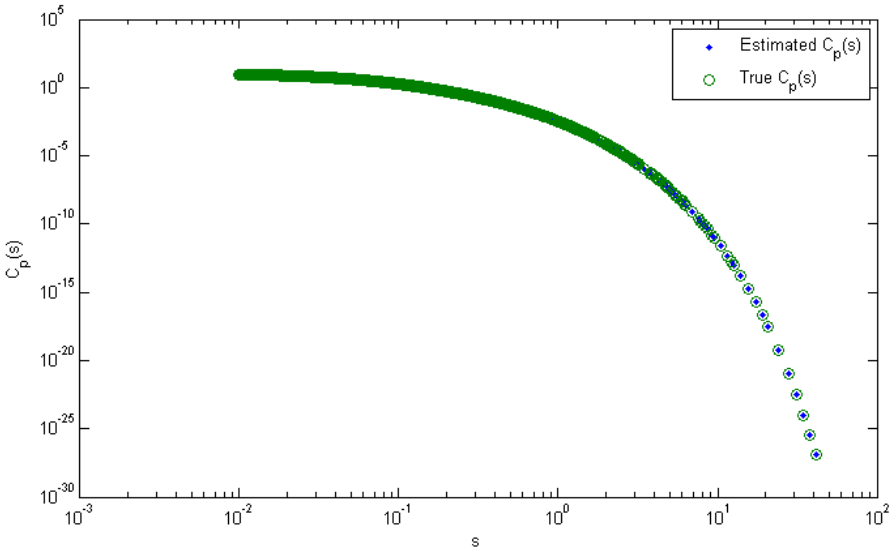

Figure 1.15: Reproduction of the tracer production data using solving the least squares problem without any regularization terms.

It was not surprising that we were able to fit the production data to such great accuracy since our problem was highly underdetermined. The more interesting thing however was that the kernel estimates that came out did not equal to the true solution, but they did fulfill the constraints in Equation (1.24). This was confirmed by successive numerical differentiation of the outcome. A log-log plot of the true kernels and the kernel estimates is shown in Figure 1.16.

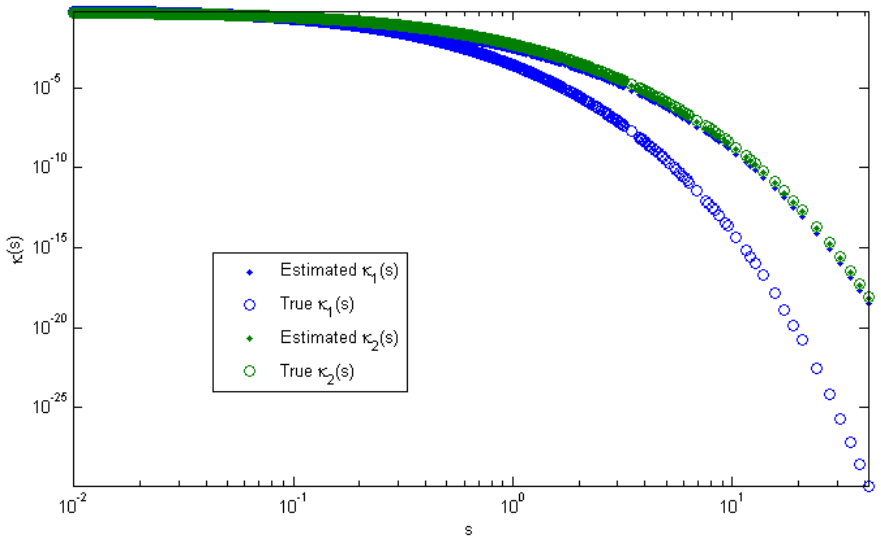

Figure 1.16: The kernel estimates did not match the true kernels very well in Laplace space, when using the pseudoinverse solution. However, the smoothness constraint (1.24) was fulfilled.

In the case shown here the data were matched perfectly, and the smoothness of the solution was in line with Equation (1.24). Thereby it was clear that this regularization method would not be sufficient to constrain the solution to a realistic estimate of the tracer kernel. The estimated kernels were converted with the Stehfest algorithm to view the solution in real space (Figure 1.17). As expected, the match was poor. The Stehfest inversion could not be blamed for this mismatch, since the Stehfest method would work well if we tested it with the true kernel data in Laplace space.

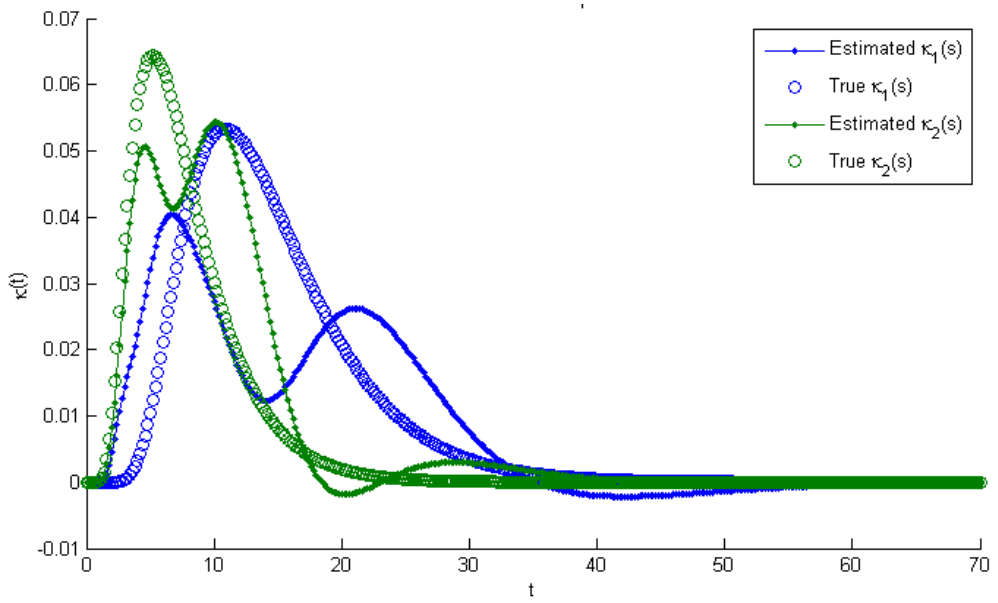

Figure 1.17: Estimated and true kernels in real space. The estimate kernels were converted from Laplace space using the Stehfest algorithm.

Using these kernel estimates to reproduce the production data in real space showed (Figure 1.18), that a good fit is obtained for the early time data, but the fit gradually worsened at later times. This was due to the nature of the Laplace transform. The Laplace transform retained information from early time data for all ranges of *s*, but for large *s* values, most of the late time information was suppressed and accuracy for late time inversions was lost.

One final problem we encountered with this method was getting an accurate forward transform of the production data. We tried computing the forward transform, using the trapezoidal rule to approximate the definition of the Laplace transform. No noise was added to the production data. When inverting the outcome back to real space (using either the Stehfest or Den Iseger method) we obtained completely erratic results. Perhaps better results could have been obtained using a more sophisticated integration method (e.g. Gaussian quadrature based) but at this point we did not see reason to investigate that challenge, nor the complications of the effects of added noise.

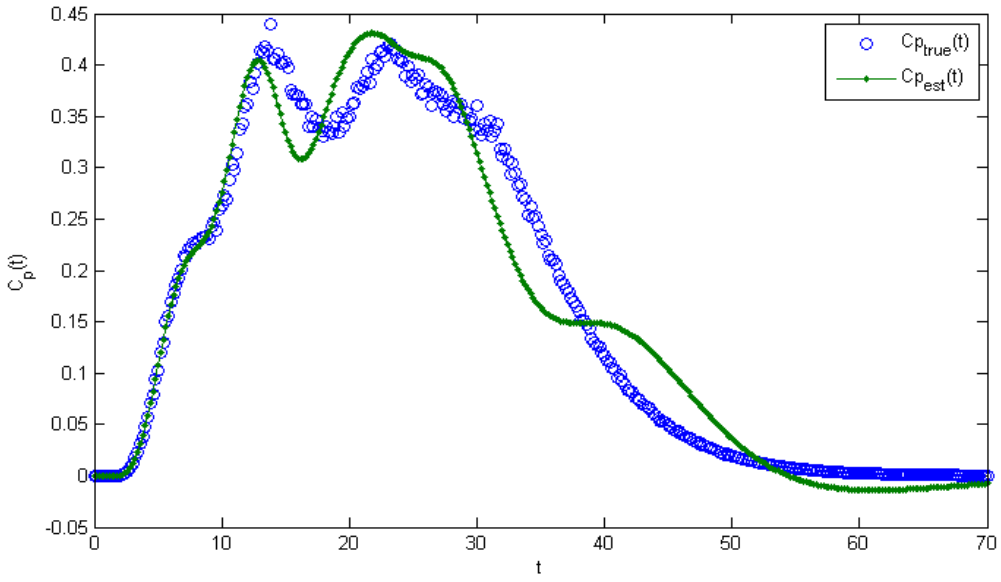

Figure 1.18: The reproduction of the production data was poor at late times using the kernel estimates shown in Figure 1.17.

1.4.2 Deconvolution based on a one-dimensional advection-dispersion equation model

This section describes a parametric approach to solving the multiwell deconvolution problem. Although it is not particularly flexible, the approach gives a more complete picture of the methods that could be used, and complements the work we have done so far using nonparametric methods.

The problem still involved finding the best estimate of the kernel functions $\kappa_k(t)$, which solve Equation (1.19). As before, we treated this as a least-squares minimization problem (1.29), but the kernels were restricted to the functional form of Equation (1.31). We were searching for the values of the parameters, $t_{a,k}$, $t_{d,k}$ and f_k, which gave the best fit of the model to the production data.

$$\begin{aligned} &\underset{\vec{\alpha}}{\text{minimize}} \quad F(\vec{\alpha}) = \frac{1}{2}\left(\vec{c}_p - \sum_{k=1}^{N_r} C_{r,k}\vec{\kappa}\right)^T \left(\vec{c}_p - \sum_{k=1}^{N_r} C_{r,k}\vec{\kappa}\right) \\ &\text{subject to} \quad \vec{\alpha} \geq 0 \end{aligned} \tag{1.29}$$

Here the kernel and production data time series are represented as vectors, $\vec{\kappa}$ and $\vec{c}_p$ and the injection data are now included in the matrix $C_{r,k}$ which represents the convolution (approximated by the trapezoidal rule).

$$C_{r,k}=\begin{bmatrix} 0 & & \cdots & & 0 \\ (\tau_2-\tau_1)c_{r,k}(t_2-\tau_1) & (\tau_2-\tau_1)c_{r,k}(t_2-\tau_2) & 0 & \cdots & 0 \\ (\tau_2-\tau_1)c_{r,k}(t_3-\tau_1) & (\tau_3-\tau_1)c_{r,k}(t_3-\tau_2) & (\tau_3-\tau_2)c_{r,k}(t_3-\tau_3) & & \vdots \\ \vdots & \vdots & \vdots & \ddots & 0 \\ (\tau_2-\tau_1)c_{r,k}(t_N-\tau_1) & (\tau_3-\tau_1)c_{r,k}(t_N-\tau_2) & (\tau_4-\tau_2)c_{r,k}(t_N-\tau_3) & \cdots & (\tau_N-\tau_{N-1})c_{r,k}(t_N-\tau_N) \end{bmatrix} \quad (1.30)$$

The vector, $\vec{\alpha}=\left[t_{a,1},t_{d,1},f_1,...,t_{a,N_r},t_{d,N_r},f_{N_r}\right]^T$ holds the parameters with respect to which we want to minimize the problem. The kernels being considered were of the form

$$\kappa_k(t)=\frac{f_k}{\sqrt{4\pi t_{d,k}t}}\exp\left[-\frac{(t_{a,k}-t)^2}{4t_{d,k}t}\right] \quad (1.31)$$

Equation (1.29) describes a nonlinear least squares minimization problem. To solve it efficiently we computed the gradient and the Hessian. The gradient was computed as:

$$\frac{\partial F(\vec{\alpha})}{\partial\vec{\alpha}}=\begin{bmatrix} \left(C_{r,1}\dfrac{\partial\kappa_1}{\partial\alpha_1}\right)^T \\ \left(C_{r,1}\dfrac{\partial\kappa_1}{\partial\alpha_2}\right)^T \\ \vdots \\ \left(C_{r,N_r}\dfrac{\partial\kappa_{N_r}}{\partial\alpha_{3N_r}}\right)^T \end{bmatrix}\left(\vec{c}_p-\sum_{k=1}^{N_r}C_{r,k}\vec{\kappa}_k\right)=V^T\Delta\vec{c}_p \quad (1.32)$$

Similarly, the Hessian was computed as:

$$\frac{\partial^2 F(\vec{\alpha})}{\partial \vec{\alpha}^2} = \begin{bmatrix} \left(C_{r,1}\frac{\partial^2 \kappa_1}{\partial \alpha_1^2}\right)^T & \left(C_{r,1}\frac{\partial^2 \kappa_1}{\partial \alpha_1 \partial \alpha_2}\right)^T & \left(C_{r,1}\frac{\partial^2 \kappa_1}{\partial \alpha_1 \partial \alpha_3}\right)^T & \vec{0}^T & \cdots & \vec{0}^T \\ \left(C_{r,1}\frac{\partial^2 \kappa_1}{\partial \alpha_2 \partial \alpha_1}\right)^T & \left(C_{r,1}\frac{\partial^2 \kappa_1}{\partial \alpha_2^2}\right)^T & \left(C_{r,1}\frac{\partial^2 \kappa_1}{\partial \alpha_2 \partial \alpha_3}\right)^T & \vec{0}^T & \cdots & \vdots \\ \left(C_{r,1}\frac{\partial^2 \kappa_1}{\partial \alpha_3 \partial \alpha_1}\right)^T & \left(C_{r,1}\frac{\partial^2 \kappa_1}{\partial \alpha_3 \partial \alpha_2}\right)^T & \left(C_{r,1}\frac{\partial^2 \kappa_1}{\partial \alpha_3^2}\right)^T & \vec{0}^T & \cdots & \\ \vec{0}^T & \vec{0}^T & \vec{0}^T & \ddots & & \left(C_{r,N_r}\frac{\partial^2 \kappa_{N_r}}{\partial \alpha_{3N_r-1} \partial \alpha_{3N_r}}\right)^T \\ \vec{0}^T & \cdots & & \left(C_{r,N_r}\frac{\partial^2 \kappa_{N_r}}{\partial \alpha_{3N_r} \partial \alpha_{3N_r-1}}\right)^T & & \left(C_{r,N_r}\frac{\partial^2 \kappa_{N_r}}{\partial \alpha_{3N_r}^2}\right)^T \end{bmatrix} \otimes \left(\bar{c}_p - \sum_{k=1}^{N_r} C_{r,k}\bar{\kappa}_k\right)$$

$$+ \begin{bmatrix} \left(C_{r,1}\frac{\partial \kappa_1}{\partial \alpha_1}\right)^T \\ \left(C_{r,1}\frac{\partial \kappa_1}{\partial \alpha_2}\right)^T \\ \vdots \\ \left(C_{r,N_r}\frac{\partial \kappa_{N_r}}{\partial \alpha_{3N_r}}\right)^T \end{bmatrix} \begin{bmatrix} C_{r,1}\frac{\partial \kappa_1}{\partial \alpha_1} & C_{r,1}\frac{\partial \kappa_1}{\partial \alpha_2} & \cdots & C_{r,N_r}\frac{\partial \kappa_{N_r}}{\partial \alpha_{3N_r}} \end{bmatrix} \tag{1.33}$$

$$= H_2 \otimes \Delta\vec{c}_p + V^T V$$

To accelerate convergence, the matrix H_2 was set to zero, in accordance with Gauss' modification to Newtons method. The derivatives of the kernel functions with respect to α_i, were computed automatically using the Symbolic Toolbox in MATLAB. The MATLAB function fmincon was then used to solve problem (1.29), using the trust region reflective algorithm. The objective function had a number of local minima and therefore it was necessary to try a few different initial guesses to get convergence to the known "true" solution. An example with five injectors and one producer is shown in Figure 1.19. As before we used somewhat idealized injection histories to make the problem better posed.

Convergence to the "true" minimum was achieved after 16 trials with random initial guesses for $\vec{\alpha}$. Each trial computation took only a few seconds (~10-30 sec) to run in MATLAB. A comparison between the true kernels and the estimated kernels is shown in the top part of Figure 1.20 and the fit to the production data is shown on the lower graph. Table 1.1 shows the parameter estimates and the true parameters used.

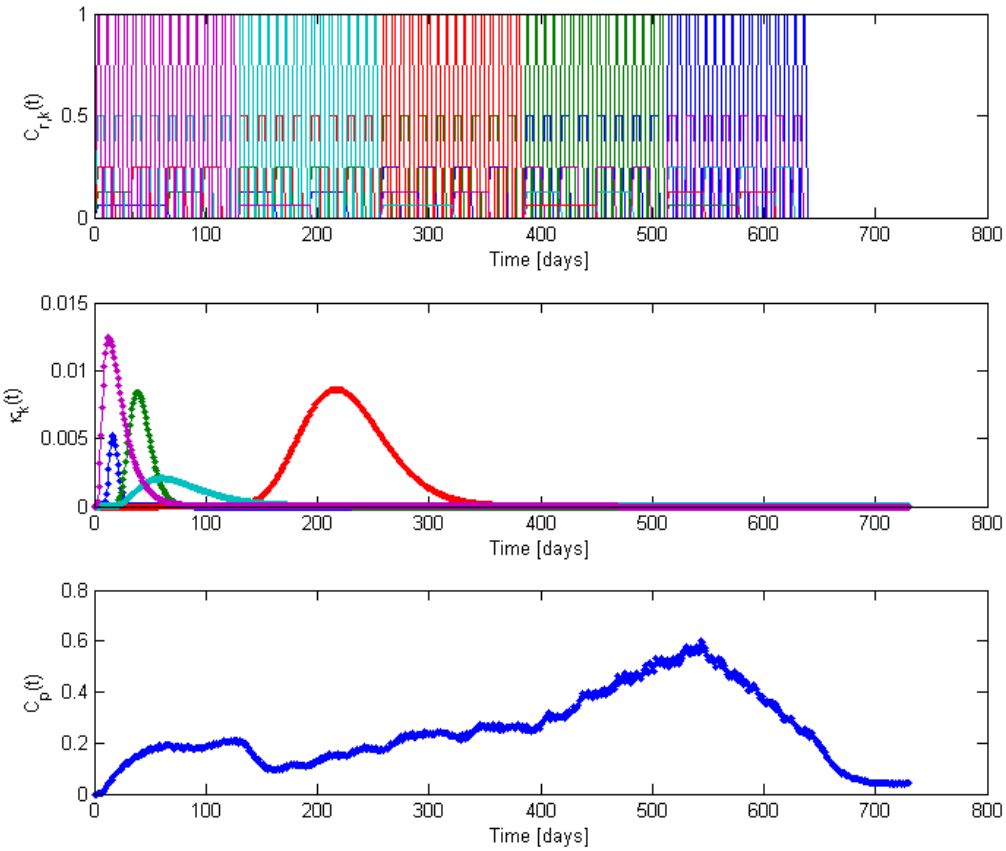

Figure 1.19: Injection history, random kernels and corresponding production history for five injectors and one producer.

Table 1.1: Summary of parametric estimates for fit shown in Figure 1.20.

	$t_{a,true}$	$t_{a,est}$	$t_{d,true}$	$t_{d,est}$	f_{true}	f_{est}
κ_1	17.1	16.9	0.43	0.56	0.05	0.06
κ_2	40.0	40.5	1.14	1.05	0.20	0.20
κ_3	220.0	219.4	3.14	3.18	0.80	0.80
κ_4	66.7	67.1	6.67	6.22	0.15	0.15
κ_5	16.0	15.9	3.20	3.14	0.30	0.30

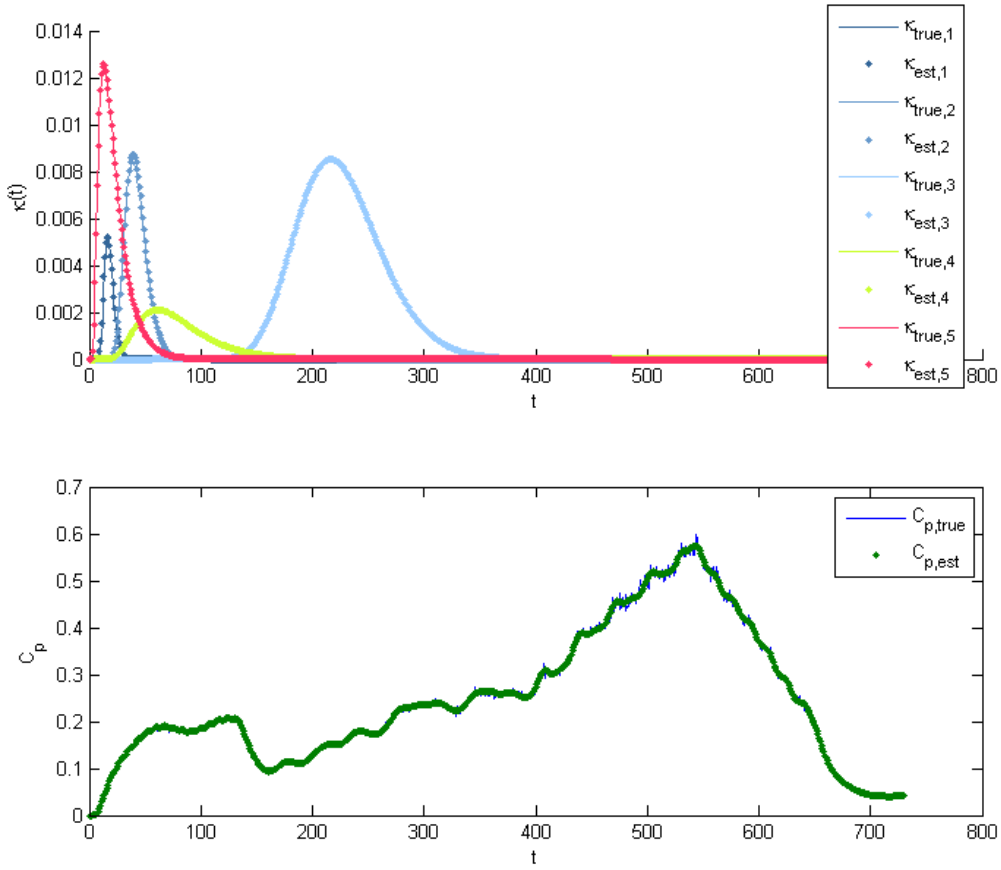

Figure 1.20: The estimation of five kernels and the fit to production data after solving problem (1.27) with a good initial guess.

Admittedly, the case shown here did yield an unrealistically good fit because the production history was generated with the same model as we were trying to fit to the data. In reality the kernels could be more like the ones shown in Figures 1.8 or 1.11, and therefore kernel models with sums two (or even three) simple kernels might be more appropriate. That is, in stead of considering kernels of the form (1.31) one might want to use:

$$\kappa_k(t) = \frac{f_{1,k}}{\sqrt{4\pi t_{d1,k} t}} \exp\left[-\frac{(t_{a1,k}-t)^2}{4t_{d1,k}t}\right] + \frac{f_{2,k}}{\sqrt{4\pi t_{d2,k} t}} \exp\left[-\frac{(t_{a2,k}-t)^2}{4t_{d2,k}t}\right] \tag{1.34}$$

When poor initial guesses to the solution were made the minimization algorithm would converge to a local minimum with results such as those shown in Figure 1.21.

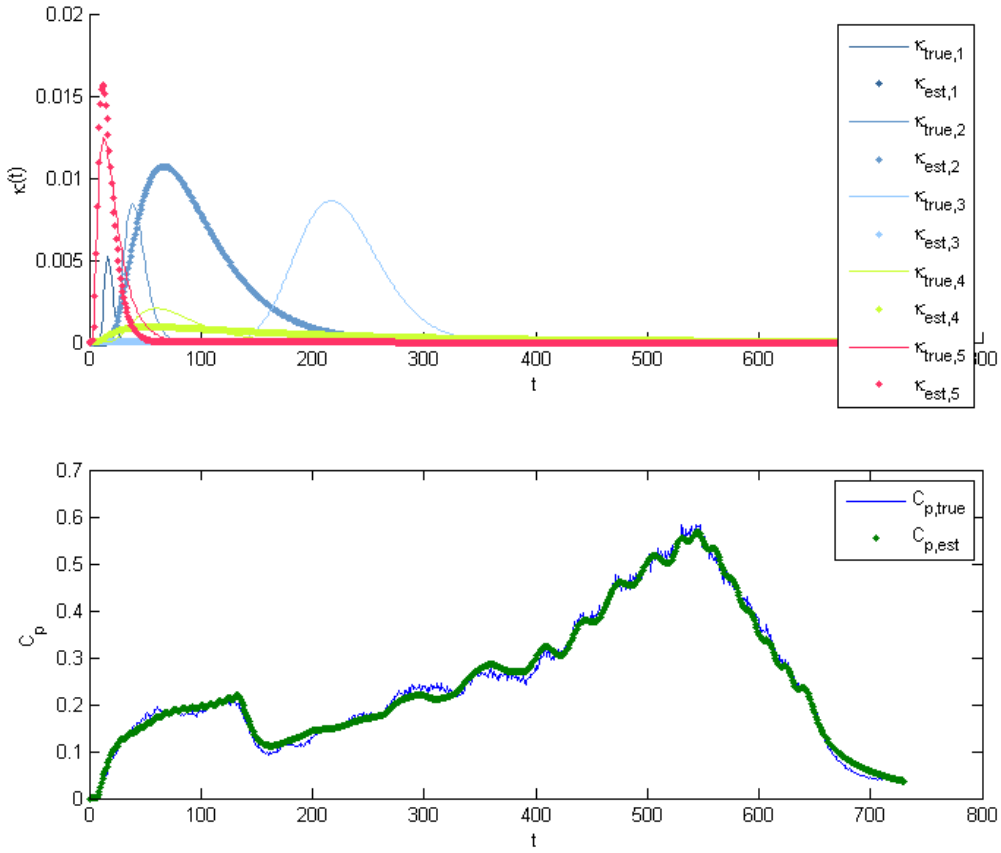

Figure 1.21: Results showing a solution of problem (1.29) with convergence to a local minimum. Even though the fit to the production data might seem quite good, the kernel estimates could be quite far off.

The problem of needing a good initial guess could be combated in a few different ways. Transformations of the parameter space might be helpful, e.g. by searching for *log(α)* in cases where α is believed to be log-normally distributed; or by modifying problem (1.29) into a total least-squares problem, where the combination of the distances in t and c_p are being minimized. We experimented with the idea of a logarithmic transformation of the parameter space for t_a and t_d with no obvious improvements, but the testing was not rigorous. The total least-squares approach would require more work, but for many practical purposes, trying a few initial guesses would be a satisfactory approach.

1.5 FUTURE WORK

Future work will focus on additional analyses of production histories. Possibilities of using the tracer response to optimize production are being considered. A straightforward approach to this would be to attempt to minimize the amount of tracer produced over a specific time interval. This could be accomplished by evaluating the tracer kernels at several different injection rates and from that trying to guess what the kernels would look

like at other intermediate injection rates. Alternative approaches might also be considered such as attempting find the injection rates that minimize the variability in the tracer production signal. The ACE algorithm, discussed in the quarterly report from Winter 2009, may lend itself well to this type of analysis.

To further our work of inferring of well-to-well connectivity, we have considered shifting the focus from tracers to pressure data. Nonparametric multiwell deconvolution approaches of pressure data have been discussed by Levitan (Levitan, 2006) and von Schroeter and Gringarten (Schroeter and Gringarten, 2007). Knowing both the tracer kernel and the pressure kernel for well-to-well connections could then be used to optimize injection schedules where the objective would be to provide maximal pressure support for production at the same time as the possibility of premature breakthrough would be minimized.

An important difference between working with pressure and tracer deconvolution is that for pressure the injection rates can (and must) change to be able to decompose the pressure signal. Therefore, a variable injection rate test could be performed first to get a rough idea of which wells might be well connected from the pressure transients, and then that information might be used to improve the design of the tracer injection tests.

Finally, we will give some thought to whether the simplified discrete fracture network analysis approach discussed in this report and the quarterly report from Winter 2010 can be extended to compute the transport of temperature signals and/or tracer signals in three dimensions.

1.6 CONCLUSIONS

This quarterly report discusses a way to compute the transport of tracer through a fracture network, including the effects of Taylor dispersion. The method is computationally efficient and provides an interesting way of comparing the dispersion induced by the multiple paths through the fracture network as opposed to the dispersion caused by molecular diffusion in narrow flow paths (Taylor dispersion). The computations show that the degree of Taylor dispersion is very sensitive to the fracture apertures. When the fracture apertures are relatively large, it becomes more likely that Taylor dispersion will mask the fracture induced dispersion effects, precluding the possibility of discerning the number of dominant flow paths between any two wells, by means of a tracer test.

The second part of this report focuses on inference of well-to-well connectivity from tracer tests. This is a direct continuation of the work done in the quarterly reports from Winter, Spring and Summer 2009. Two methods are discussed; the first being a nonparametric deconvolution approach performed in Laplace space; and the second being a parametric deconvolution approach based on nonlinear regression with a one-dimensional advection-dispersion model. The nonparametric Laplace space method seemed to be infeasible due to the imprecise way in which late time data were represented in Laplace space. The parametric approach involved working out the gradient and Hessian of a nonlinear least squares problem. The method seemed to work well for the test case we used, aside from some nuances with getting a good initial guess for the parameters. Extensions of the

method were suggested that could improve convergence and widen the range of conditions for which the method might work.

2. FRACTURE CHARACTERIZATION OF ENHANCED GEOTHERMAL SYSTEMS USING NANOPARTICLES

This research project is being conducted by Research Associates Mohammed Alaskar and Morgan Ames, Senior Research Engineer Kewen Li and Professor Roland Horne. The objective of this study is to develop in-situ multifunction nanosensors for the characterization of Enhanced Geothermal Systems (EGS).

2.1 SUMMARY

Injection of hematite (iron oxide Fe_2O_3) nanorice was conducted to explore the mobility of rod-like nanoparticles within the pore spaces of Berea sandstone. The purpose was to investigate constraints imposed by the geometry and aggregation of the rod-like nanoparticles. Hematite nanoparticles were not identified in the effluent collected from the Berea sandstone core. The hematite nanorice was, however, detected within the pores at the inlet side of the core.

To study the transport of hematite nanorice within a porous medium in the absence of rock materials, a glass bead packed slim tube was designed and constructed. During this injection, a very small number of hematite nanoparticles were observed using SEM imaging of the effluent samples. However, the particle count was too low to be detected by UV-visual spectroscopy, so it was not possible to determine the concentration of the effluent samples.

In order to determine whether the transport of hematite nanorice is limited by their geometry or their surface characteristics, the hematite nanoparticles were coated with silica (SiO_2) and the surfactants triethanolamine (TEA) and polyvinylpyrrolidone (PVP) to modify their surface properties. The next step will be to characterize and inject the coated hematite.

Tin-bismuth (Sn-Bi) alloy nanoparticles were synthesized to begin investigating temperature-sensitive particles. However, an attempt to characterize the particles using dynamic light scattering was unsuccessful due to the presence of large particulates.

This report describes the results of the iron oxide nanoparticle injection into Berea sandstone and 30 cm glass bead packed slim tube as well as the synthesis of Sn-Bi alloy particles and the coating of hematite nanorice with surfactants.

2.2 INTRODUCTION

The last quarterly report (January-March 2010) described the injection of silicon dioxide nanoparticles into a 10m long sand-packed slim tube, and the analysis of this experiment. This included the characterization of the injected nanofluid as well as effluent samples. It was found that the silicon dioxide nanoparticles can be transported and recovered through a long flow path. To investigate the transport of nonspherical particles through porous media and to gain further experience in the synthesis of nanomaterials, a hematite (Fe_2O_3) nanofluid sample was synthesized and characterized using scanning electron microscopy.

In this quarter, hematite nanorice injection experiments were carried out using Berea sandstone and a glass bead packed slim tube. Influent and effluent samples were analyzed using dynamic light scattering, UV-visual spectroscopy and scanning electron microscopy. Standard measurements on the core sample were also performed. These measurements included the gas and liquid permeability, porosity and pore volume measurements. To better understand the relationship between particle geometry and transport, the hematite was coated with SiO_2 and the surfactants TEA and PVP. Finally, the investigation of temperature-sensitive nanoparticles began with the synthesis of Sn-Bi alloy nanoparticles.

2.3 BEREA SANDSTONE AND GLASS BEAD PACKED SLIM TUBE CHARACTERIZATION

This section describes the porosity, permeability and pore volume measurements of Berea sandstone and slim tube packed with glass beads used in the hematite nanorice injection experiments.

2.3.1 Berea Core Characterization

The core sample tested was Berea sandstone of 3.8 cm in diameter and 4.9 cm in length. The gas and liquid permeabilities were determined. The Klinkenberg (gas slippage) effect was considered to evaluate the equivalent liquid permeability. Then, the liquid permeability for the same core sample was carried out. Porosity and permeability results are summarized in Table 2.1.

Table 2.1: Berea porosity and permeability measurements summary

Property	**Measurement method**	**Value**
Porosity (%)	Saturation with deionized water	17.1
Permeability (md)	Gas permeability	152
	Equivalent liquid permeability	72.2
	Liquid permeability	60.7

Figure 2.1 is a schematic of the apparatus used in the measurement of gas permeability. The gas used in this experiment was nitrogen (N_2). The inlet and outlet pressures were measured using standard pressure gauges. The flow rate at the outlet was measured using a stop-watch and graduated cylinder (the standard method of measuring the flow rate). Calibration curves were included in an earlier quarterly report (January-March 2009).

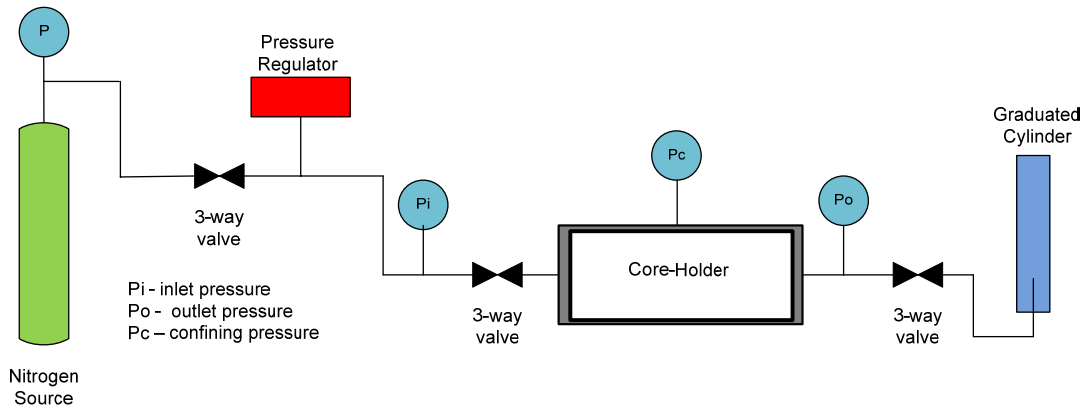

Figure 2.1: Schematic of the apparatus for measuring gas permeability.

The core was first dried in a furnace at 100°C under vacuum for 24 hours. After weighing the core sample, it was placed inside the core-holder under a confining pressure of 450 psig. The gas permeability measurement was then started by introducing nitrogen at different flow rates and inlet pressures. The average gas permeability was found to be around 152 millidarcy by applying Darcy's law for compressible fluids:

$$k_{gas} = \frac{2\mu p_{out} q_{out} L}{A(p_{in}^2 - p_{out}^2)} \tag{2.1}$$

where μ is the viscosity in centipoise, q_{tot} is outlet volumetric flow rate in cubic centimeter per second, A is the core cross-sectional area in square centimeter, L is the core length in centimeter and p_{in} and p_{out} are inlet and outlet absolute pressures in atmospheres, respectively.

The gas permeability as a function of the reciprocal of mean pressure is depicted in Figure 2.2. According to the Klinkenberg effect, extrapolating the straight line to infinite mean pressure (or zero reciprocal of mean pressure) intersects the permeability axis at a point designated as the equivalent liquid permeability (Amyx et al., 1960). In Figure 2.2, the average equivalent liquid permeability is approximately 72.2 millidarcy.

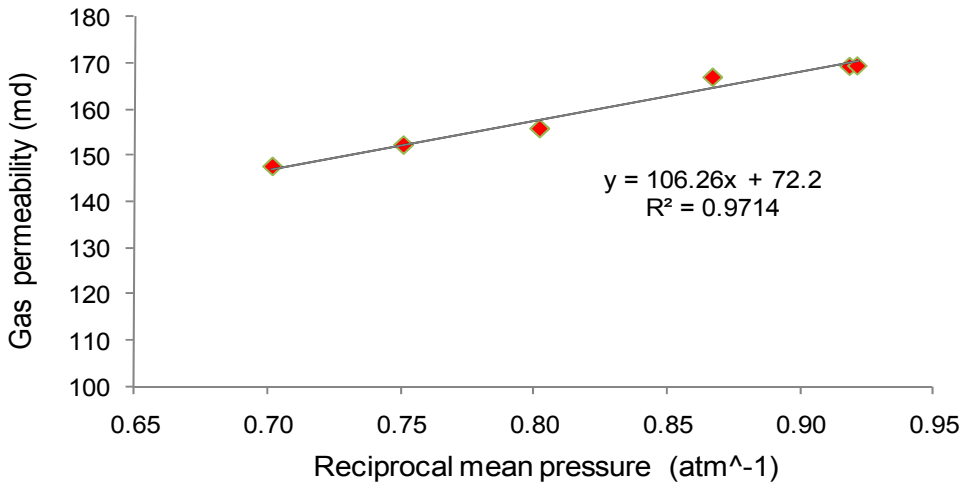

Figure 2.2: Berea core gas permeability versus the reciprocal of mean pressure.

The liquid permeability was measured on the same core sample directly. A schematic of the apparatus used in the measurement of liquid permeability is shown in Figure 2.3.

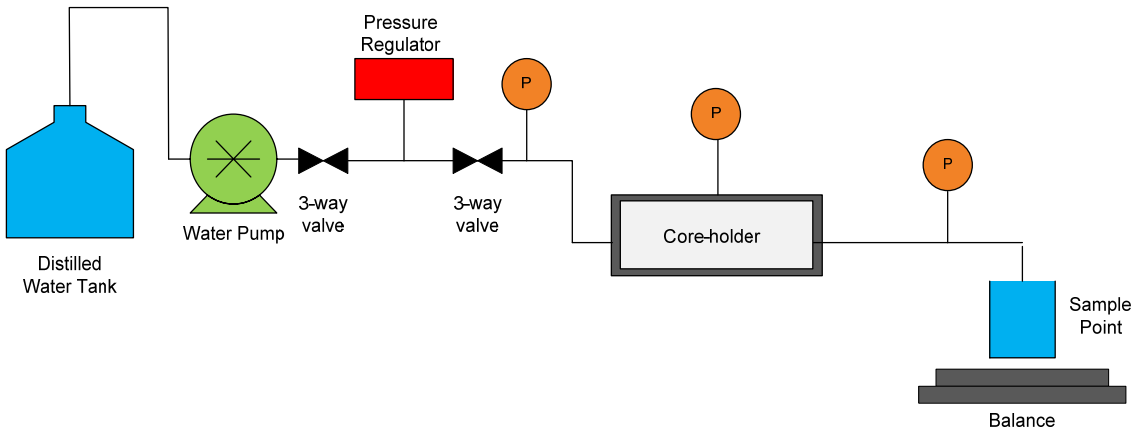

Figure 2.3: Schematic of apparatus for liquid permeability measurement.

The core sample was first saturated with water outside the core-holder. The core and related system were evacuated using a Welch Vacuum Pump for 4 hours at a vacuum pressure of about 20 millitorr to remove moisture. Pure water was introduced to completely submerge the sample. The core was then left submerged overnight and the remaining vacuum released to aid the process of saturation. After that the core was removed and wiped dry to remove excessive water on the surface. Finally, the core was weighed and hence its porosity was calculated. The core turned out to have a porosity of around 17.1 % and a pore volume of 9 cubic centimeters. The porosity calculation is as follows:

$$\phi = \frac{V_p}{V_B} * 100 \tag{2.2}$$

$$V_p = W_s - W_d \tag{2.3}$$

$$V_B = \pi r^2 l \tag{2.4}$$

where ϕ is the porosity in percentage, V_p and V_B are pore and bulk volumes in cubic centimeter, respectively. W_s and W_d are the weight of core after and before saturation, in gram, respectively. r and l are the radius and length of the core in centimeter, respectively.

The average liquid permeability was found to be around 60.7 millidarcy. Darcy's law for horizontal flow was utilized to compute the permeability. Darcy's law for horizontal flow is given by:

$$k_{liq} = \frac{q\mu L}{A\Delta p} \tag{2.5}$$

where q is the volumetric flow rate in milliliter per second, μ is the viscosity in centipoise, L and A are the length and the cross-sectional area of the core in centimeter and square centimeter, respectively. Δp is the differential pressure across the core sample in atmospheres.

2.3.2 Polypropylene slim tube packed with glass beads

To investigate the mobility of hematite nanoparticles in the absence of rock material (such as clays), they were injected into a slim tube packed with glass beads. A 30 cm long polypropylene slim tube apparatus was constructed. The tube was packed with glass beads of 1 mm diameter and fitted with filter paper, screens, and valves at each end. This polypropylene slim tube is pictured in Figure 2.4. The porosity was measured by the resaturation method. The porosity and pore volume of the glass bead packed slim tube were found to be approximately 47% and 2.5 ml, respectively.

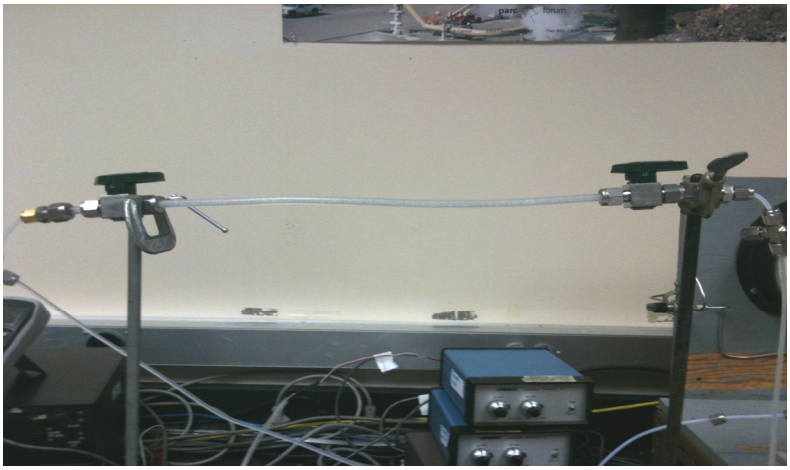

Figure 2.4: Polypropylene slim tube packed with glass beads

2.4 HEMATITE INJECTION EXPERIMENTS

During this quarter, two main experiments were conducted. They serve as preliminary testing of the injection of hematite nanorice into Berea sandstone and into the slim tube packed with glass beads. The injection process and sampling strategies in both experiments were similar; however, they differ in some aspects such as total Pore Volume Injected (PVI), flow rates and sampling frequency. The following sections provide the specifics of each experiment.

2.4.1 Hematite nanoparticle injection into Berea sandstone

Injection of hematite (iron oxide Fe_2O_3) nanorice was conducted to investigate their flow through the pores of Berea sandstone. A schematic of the apparatus is shown in Figure 2.5. Nanofluid solution was contained in a pressure vessel downstream of the water pump. The hematite nanorice was injected with the aid of nitrogen gas. The configuration also allows for injection of particle-free water, without interrupting the flow.

This experiment did not consider the temperature effect, so it was conducted at room temperature. The nanofluid contained hematite nanoparticles of the size of 500 nm in length and 100 nm in diameter.

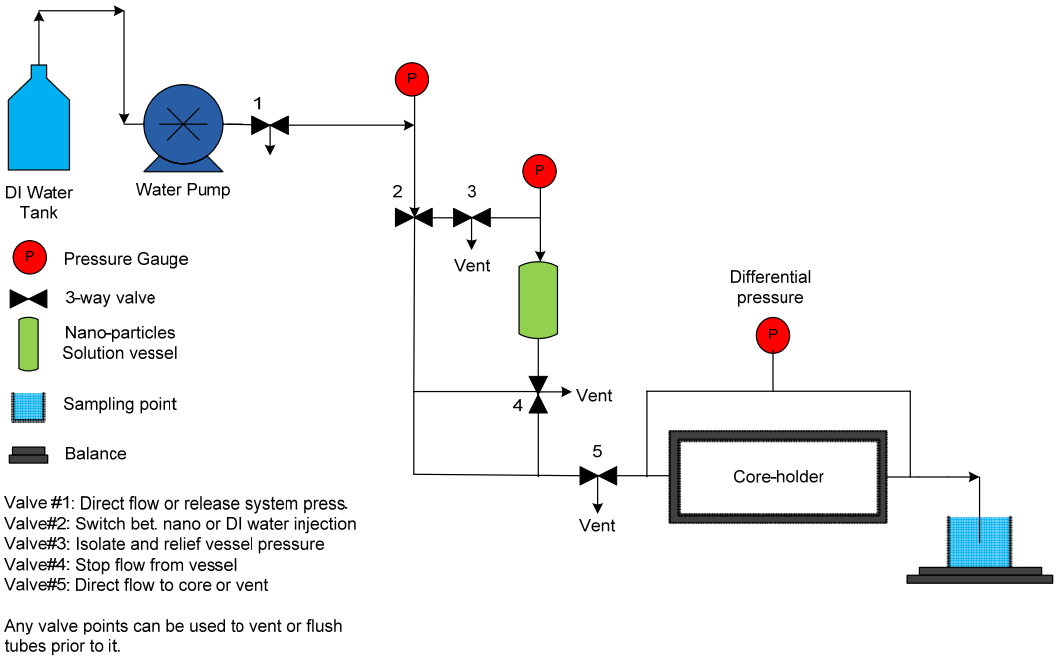

Figure 2.5: Experimental apparatus for nanofluid injection into Berea sandstone.

Prior to the injection of the nanofluid, the core was preflushed with pure water to displace as much rock fines and debris as possible. The nanofluid injection sequence was similar to the process suggested by Kanj et al. (2009). The sequence involved the injection of a specified volume of nanofluid followed by a continuous injection of pure water. In

particular, 40% of the pore volume was injected. The hematite nanofluid was diluted 1:10 (i.e. 1 part hematite to 10 parts pure water).

Subsequent to the injection of the nanofluid, a continuous flow of pure water (post injection) was introduced. Specifically, 8 pore volumes of pure water were injected while the effluent samples were collected. The total time of the experiment was approximately 40 minutes. The injection was at the rate of 2 milliliter per minute at a differential pressure of about 6 psig. A total of 17 effluent samples were collected at the rate of 3 milliliter per sample. Not all these samples were analyzed but rather a selection of some was made to reduce the analysis time. In that regard, samples from the second and fourth post injected pore volume where analyzed by SEM.

2.4.2 Hematite nanoparticle injection into glass bead packed slim tube

The hematite nanorice was also injected into slim tube packed with glass beads. The same experiment configuration (Figure 2.5) was used except that the coreflooding apparatus was replaced with a 30 cm long, 0.635 cm diameter polypropylene slim tube packed with spherical glass beads. The same hematite sample injected into the Berea sandstone was used in the glass beads injection experiment.

The slim tube was initially preflushed with several pore volumes using pure water. Then, three different injections of hematite nanofluid, each followed with continuous injection of pure water (post injection) were conducted. In each experiment, the volume of hematite injected was about 40% of the pore volume (or 1 ml nanofluid). During the first injection, the hematite nanofluid was diluted (1 part of hematite to 10 parts pure water). In the second and third injections, the hematite nanofluid was not diluted. However, it was observed that the paper filters fitted at the tube inlet and outlet had clogged with the nanorice (Figure 2.6) and therefore the filters were removed prior to the third injection.

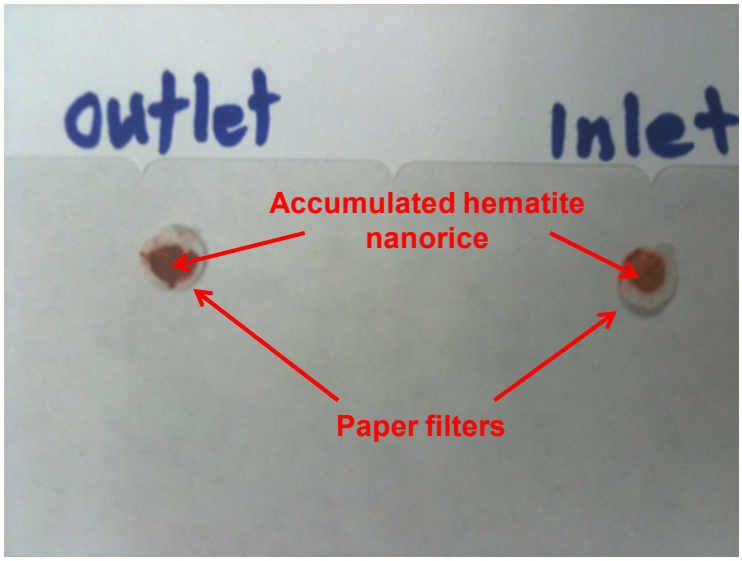

Figure 2.6: Paper filters fitted to inlet and outlet valves during hematite injection experiment. The filters were removed prior to the third injection of hematite.

2.5 COATING OF HEMATITE NANOPARTICLES

After early results indicated a difficulty in getting the hematite particles to pass through the core, it was postulated that their elongated shape caused them to have nonuniform surface potential that resulted in clustering of the particles. Because this would be a general property of rod-shaped particles, an investigation of this issue was initiated, first by coating the hematite nanorice with different materials to alter their surface charges.

Hematite was coated with SiO_2 and the surfactants triethanolamine (TEA) and polyvinylpyrrolidone (PVP) in order to modify its surface properties and determine if transport is limited by geometry or surface properties.

SiO_2 was particularly attractive as a coating because it has already been injected into a core and recovered successfully. To perform this coating, 0.3 ml of hematite nanofluid suspended in water was diluted with 4 ml of water and 20 ml of ethanol, a slight variation of the process suggested by Lu (2002). 0.5 ml of 30 wt % ammonia solution and tetraethyl orthosilicate (TEOS) were added while the solution was stirred magnetically, and the reaction continued for 3 hours at room temperature. The coated nanorice were separated from the reaction medium via centrifugation and suspended in water.

To coat the hematite with PVP, a 0.1 M solution of PVP in ethanol was prepared. Hematite nanofluid was then added, sonicated for 1 hour, and soaked overnight. The coated particles were cleaned by centrifugation three times at 6.5 krpm to remove excess surfactant. The TEA coating was identical, except a 0.1 M solution of TEA in water was used instead.

2.6 TIN-BISMUTH NANOPARTICLE SYNTHESIS

To begin investigating temperature-sensitive nanoparticles, the synthesis of Sn-Bi alloy nanoparticles was performed. The ideal geothermal temperature sensor should be nontoxic, able to pass through the reservoir, easily recovered if necessary, and should undergo an easily observable change in the temperature range of interest. One promising idea is a core-shell particle with an inert, magnetic core and a shell that undergoes decomposition or phase change. One of the reasons hematite has been investigated is because of its behavior under an applied magnetic field. This would make it an ideal material for the inert core if the transport barriers can be overcome. The shell could be a metal alloy with a low melting point (i.e. within the range of common geothermal temperatures). Sn-Bi alloys could be used as sensors in the temperature range between eutectic melting point of the alloy (139°C) and the pure melting points of Bi and Sn (271°C and 232°C, respectively), as shown in Figure 2.7.

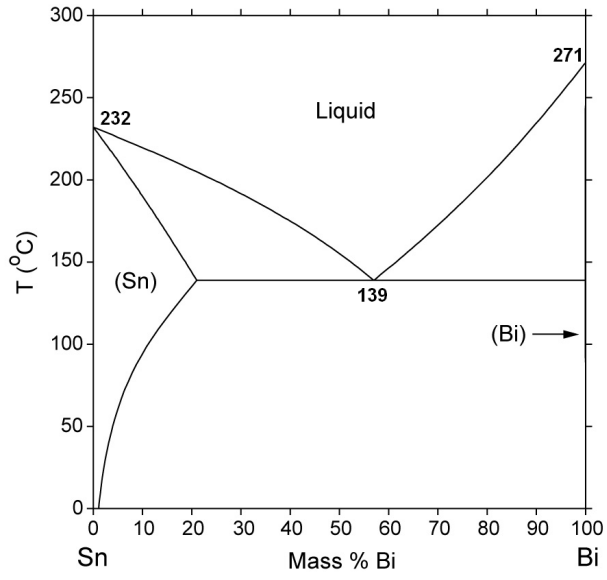

Figure 2.7: Phase diagram of Sn-Bi.
<http://www.metallurgy.nist.gov/phase/solder/bisn.html>

Moreover, the alloy is stable under ambient conditions and both metals are inexpensive and nontoxic in their metallic states (Connor, 2010). Finally, there are known processes for depositing Sn-Bi coatings, particularly on hematite core particles (Connor, 2010). The synthesis of Sn-Bi alloy nanoparticles is considered a preliminary in the creation of the envisioned core-shell nanosensors.

To perform the synthesis, Sn and Bi were melted together at the eutectic composition (~60 wt % Bi and ~40 wt % Sn). After it was cooled to room temperature, 100 mg of the alloy was sonicated in 10 ml of mineral oil, a slight variation of the sonochemical method suggested by Chen (2005). The VC-505 ultrasonic processor manufactured by Sonics & Materials, Inc. with a 0.5 in. replaceable tip was used. The sonicator was operated at 100 W (20% power) with a pulse setting of 1 s on, 10 s off. The sonicator is capable of operating at 500 W, but was not operated as such due to concerns that the organic solvent would break the replaceable tip. The mixture was cooled to room temperature and centrifuged. The alloy particles were washed several times with ethanol, and suspended in a solution of 100 mM PVP in ethanol.

An attempt was made to characterize the alloy particles using dynamic light scattering, but this was unsuccessful due to the presence of large particulates in the sample. This is most likely due to the low power setting used for the sonicator as a precaution. In order to operate at higher powers in organic solvents, a solid probe was required, so a VC-505 with a 0.75 in solid probe was purchased. This ultrasonic processor is pictured in Figure 2.8. The synthesis will be repeated using this equipment at higher power.

Figure 2.8: VC-505 ultrasonic processor (Sonics & Materials, Inc.). *<http://www.sonics.com/liquid-new-sheet/VC505-750.pdf>*

2.7 RESULTS

Injection of hematite (iron oxide Fe_2O_3) nanorice was conducted to investigate their mobility within the pore spaces of Berea sandstone. The purpose was to investigate constraints imposed by the geometry and aggregation of the rod-like nanoparticles. The nanoparticles were found to be roughly 500 nm in length and 100 nm in diameter, resulting in an aspect ratio of 5:1 (Figure 2.9). By comparison, the hematite nanorice was at least an order of magnitude shorter than the silver nanowires injected previously (quarterly report, July-September 2009). Thus, the nanorice was used to test the hypothesis made regarding the entrapment of the silver nanowires due to their geometry (length). Hematite nanorice was not identified in effluent collected during the injection into Berea sandstone. Light scattering, UV-visible spectroscopy and scanning electron microscopy were used to examine the effluent samples, in which no nanoparticles were detected. The hematite nanorice was, however, observed within the pores at the inlet side of the core as illustrated by SEM micrographs in Figure 2.10.

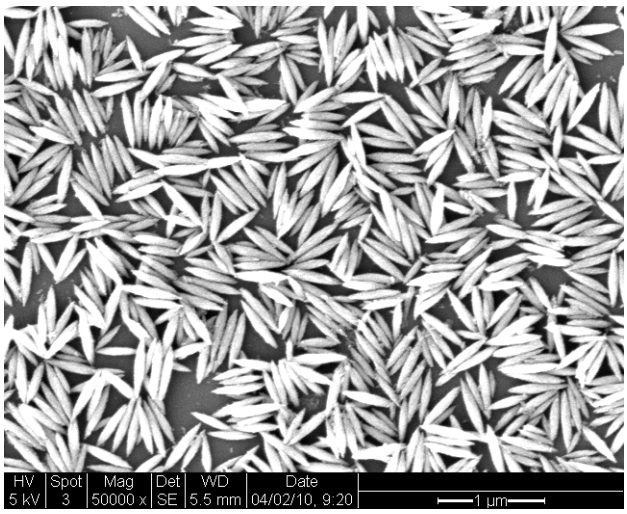

Figure 2.9: SEM image of hematite nanorice influent.

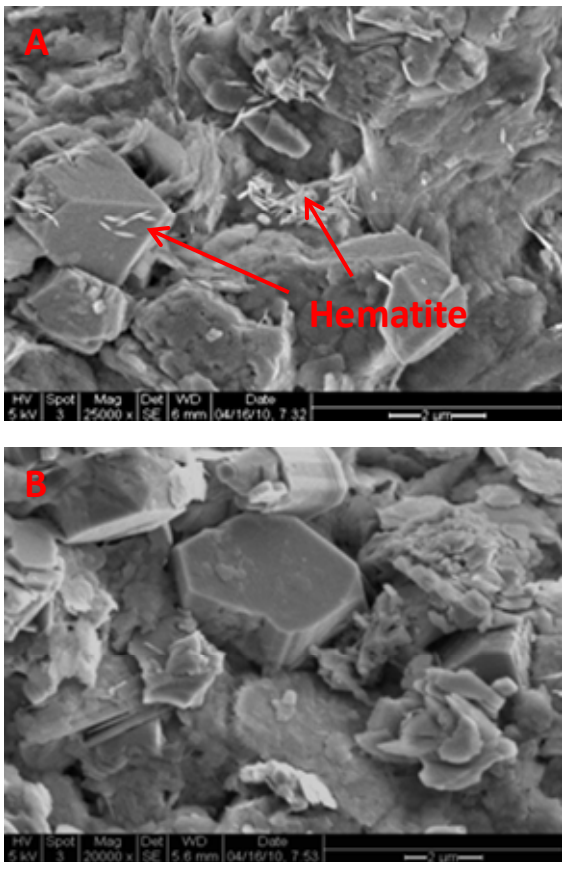

Figure 2.10: SEM imaging of Berea sandstone at (A) front side, (B) back side of the slice.

Similar to the analysis done for the silver nanowire injection, a thin slice of the core at the inlet was cut and SEM imaging was performed on both sides. Hematite nanorice was observed on the front face but not on the back face. Poulton and Raiswell (2005) reported

that the natural spherical iron oxides nanoparticles (10-20 nm) in sediments tend to aggregate at the edges of clay grains, most likely because of their surface charge characteristics. Tipping (1981) and Tipping and Cooke (1982) observed that iron oxides were negatively charged in fresh water while the edge of clay has positive charge which may explain the particle aggregation at that location. The micrographs in Figure 2.10 do not provide conclusive evidence of this interaction between the sandstone clays and the hematite nanorice. Nevertheless, this result suggested that there may be interaction between hematite nanorice and the sandstone core itself and/or among the nanorice in the form of particle aggregation. To investigate these two separate issues independently, the hematite was injected into a porous medium that consisted of a tube packed with glass beads. Spherical glass beads with a diameter of 0.1 cm were packed into a polypropylene slim tube with a diameter of 0.635 cm and a length of 30 cm.

Lecoanet et al. (2004) studied the mobility of several nanochemistry particulates in a column of tightly packed glass beads. Although all particles and the glass beads were negatively charged, the mobility of evaluated materials differed substantially from one another. For instance, 95% of injected fullerol particles were recovered rapidly as opposed to C_{60}, where less than 50% of the influent concentration was recovered.

In the case of hematite nanorice injection, both the glass beads and the hematite were negatively charged. A low particle count was observed using SEM imagery of several effluent samples at different post-injected pore volumes, as shown in Figure 2.11. The absorption of nanoparticles using UV-visible spectroscopy could not be measured due to their low concentrations, and thus the concentration of iron oxide nanoparticles in the effluent relative to the concentration in the influent also could not be determined. However, it was determined that in the absence of the clays and despite the fact that the porous medium and nanorice were carrying the same charge, the nanorice exhibited very low mobility.

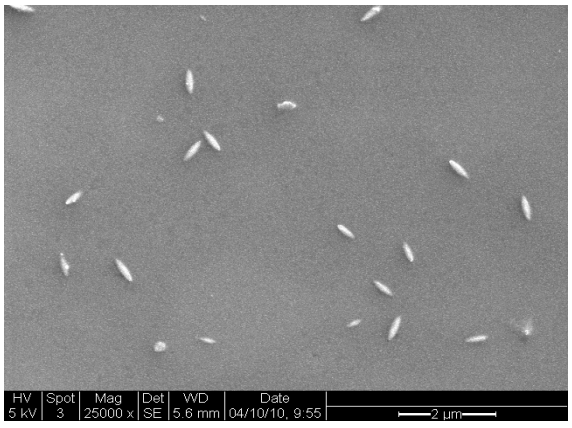

Figure 2.11: SEM image of effluent sample from the hematite glass beads injection.

The actual glass beads from the inlet and outlet were also examined under SEM (Figure 2.12). Although the hematite nanorice recovery and/or mobility were low, they were able

to flow to the outlet (about 30 cm distance). The particles were also found aggregated on the surface or within the surface defects of the glass beads themselves.

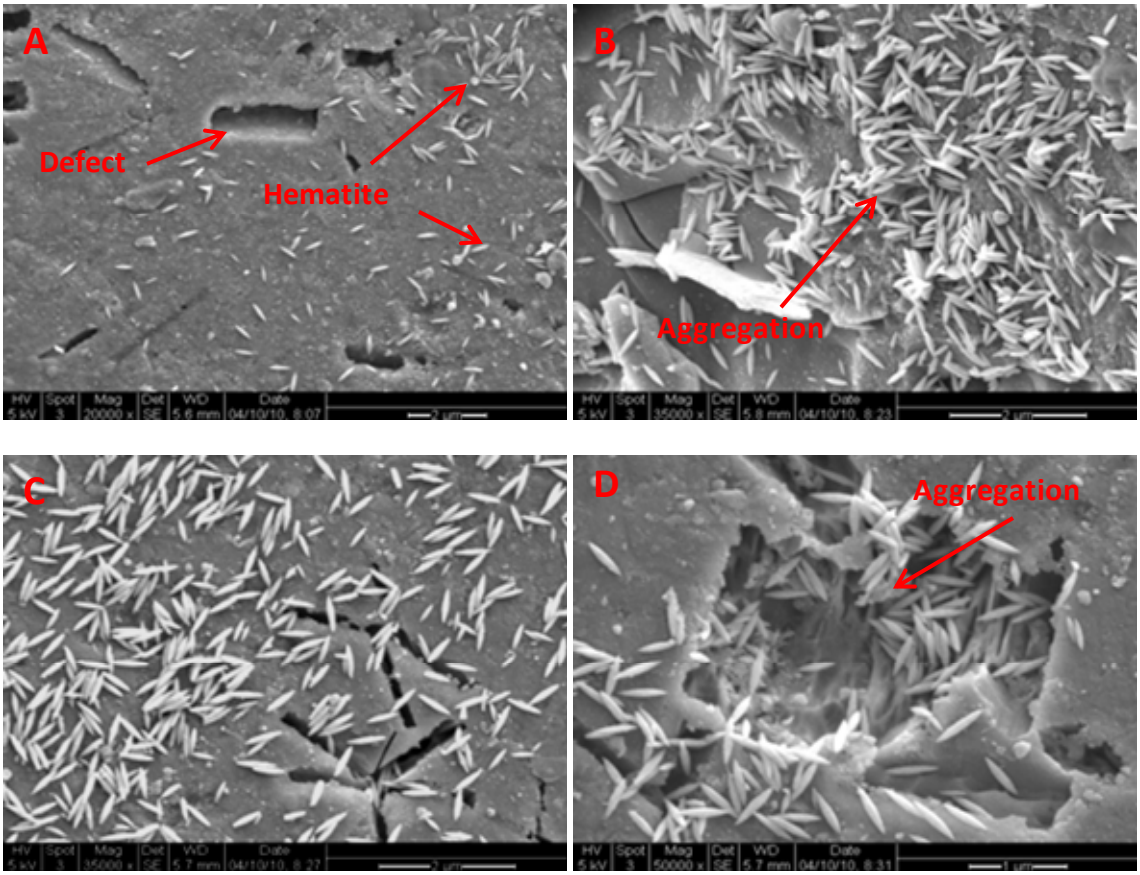

Figure 2.12: Hematite nanorice aggregation on the surface of glass beads at (A) & (B) inlet and (C) & (D) outlet side of the flow apparatus.

As can be observed in Figure 2.12, the anisotropic hematite particles have a tendency to aggregate in clusters. Lu et al. (2002) reported that iron oxide nanoparticles often aggregate in large clusters as a result of anisotropic dipolar forces. This aggregation could cause problems during transport through pore networks, such as bridging of the pores.

2.8 FUTURE WORK

The next stage will be to inject the hematite nanorice coated with PVP, TEA and SiO_2 into the 30 cm slim tube packed with glass beads. Depending on the results of this injection, the same nanofluids will be injected into Berea sandstone. The influent and effluent samples will be characterized using dynamic light scattering, UV-visual spectroscopy as well as scanning electron microscopy. The Sn-Bi synthesis will be performed again with a sonicator that has a solid probe and can be operated at higher power. Then these nanoparticles will be fully characterized, and their melting behavior at different temperatures will be investigated.

3. FRACTURE CHARACTERIZATION USING RESISTIVITY

This research project is being conducted by Research Assistant Lilja Magnusdottir, Senior Research Engineer Kewen Li and Professor Roland Horne. The objective of this project is to investigate ways to use resistivity to infer fracture properties in geothermal reservoirs.

3.1 SUMMARY

The aim of this part of the project is to use resistivity measurements and modeling to characterize fracture properties. The resistivity distribution in the field can be estimated by measuring potential differences between various points and the resistivity data can be used to infer fracture properties due to the large contrast in resistivity between water and rock.

A two-dimensional model has been made to calculate a potential field due to point sources of excitation. The model takes into account heterogeneity by solving the potential field for inhomogeneous resistivity. Fractures are modeled as areas with resistivity different from the rock, to investigate the changes in the potential field around them. In the third phase of the project, which this report mainly discusses, the model is improved to solve the potential field for a nonuniform rectangular grid. The fracture elements can be modeled smaller than the elements for the rest of the reservoir, in order to decrease the total number of elements.

The potential difference is calculated for a large number of fracture patterns, to investigate whether the results can be used to imply a pattern for an unknown field. The statistics give a better estimate of the fracture field by eliminating a great amount of possible fracture patterns for a certain potential difference. Some of the patterns have, however, similar potential differences. The possibility of using conductive fluid to enhance the contrast between fracture and rock resistivity is explored and the use of conductive fluid with time dependent resistivity measurements, in order to gain more information about the fracture properties.

A flow simulation is performed where the distribution of a tracer is observed. The tracer, which increases the conductivity of the fluid, is injected into the reservoir and future work will involve connecting the results of the flow simulation to the resistivity model. The changes of the potential field at different time steps can then be calculated as the tracer transfers through the fractures in the reservoir. Those time dependent changes in potential field as the conductive fluid flows through the fracture network facilitate fracture characterization.

3.2 INTRODUCTION

The design of optimal production strategies in geothermal reservoirs requires knowledge of the resource's connectivity and heat intensity for energy extraction. Drilling and completion of wells are expensive and the energy content from a well depends highly on the fractures it intersects. Fracture characterization is therefore important to increase the reliability of geothermal wells and thereby the overall productivity of geothermal power plants.

In this project, the goal is to find ways to use Electrical Resistivity Tomography (ERT) to characterize fractures in geothermal reservoirs. ERT is a technique for imaging the resistivity of a subsurface from electrical measurements. Typically, electrical current is injected into the subsurface through conducting electrodes and the resulting electrical potentials are measured. Due to the large contrast in resistivity between water and rock, the resistivity measurements could be efficiently used to indicate fracture locations.

Resistivity measurements have been widely used in the medical industry to image the internal conductivity of the human body, for example to monitor epilepsy, strokes and lung functions as discussed by Holder (2005). In Iceland, electrical resistivity tomography methods have been used to map geothermal reservoirs. Arnarson (2001) describes how different resistivity measurements have been efficiently used there to locate high temperature fields by using electrodes located on the ground's surface. Stacey et al. (2006) investigated the feasibility of using resistivity to measure geothermal core saturation. A direct current pulse was applied through electrodes attached in rings around a sandstone core and it resulted in data that could be used to infer the resistivity distribution and thereby the saturation distribution in the core. It was also concluded by Wang (2000) that resistivity data has high resolution power in depth direction and is capable of sensing the areal heterogeneity.

In the approach considered in this project, electrodes would be placed inside geothermal wells and the resistivity anomalies studied between them to locate fractures and infer their properties by resistivity modeling. Due to the lack of measurement points, i.e. limited number of test wells, we will endeavor to find ways to ease the process of characterizing fractures from limited resistivity data. To enhance the contrast in resistivity between the rock and fracture zones, the possibility of using conductive fluid is explored. Furthermore, the influences of temperatures and fluid stream on resistivity measurements will be studied. The effects of mineralization in the fractures will also be examined, since fractures containing a lot of minerals can be more difficult to distinguish from the surrounding rocks. This report first describes the resistivity model that has been made to calculate a potential field due to point sources of excitation and then discusses the attempt to use that model to characterize different fractures patterns.

3.3 RESISTIVITY MODELING

One of the main problems in resistivity modeling is to solve the Poisson's equation that describes the potential field and to efficiently complete the inversion iteration. That governing equation can be derived from some basic electrical relationships as described by Dey and Morrison (1979). Ohm's Law defines the relationship between current density, J, conductivity of the medium, σ, and the electric field, E, as

$$J = \sigma E \tag{3.1}$$

The stationary electric fields are conservative, so the electric field at a point is equal to the negative gradient of the electric potential there, i.e.

$$E = -\nabla \phi \tag{3.2}$$

where ϕ is the scalar field representing the electric potential at the given point. Hence,

$$J = -\sigma \nabla \phi \tag{3.3}$$

Current density is the movement of charge density, so according to the continuity equation, the divergence of the current density is equal to the rate of change of charge density,

$$\nabla J = \frac{\partial Q(x,y,z)}{\partial t} = q(x,y,z) \tag{3.4}$$

where q is the current density in amp m^3. Combining Equations (3.3) and (3.4) gives the following Poisson's equation which describes the potential distribution due to a point source of excitation,

$$\nabla[\sigma \nabla \phi] = -q(x,y,z) \tag{3.5}$$

The conductivity σ is in mhos m^{-1} and the electric potential is in volts. This partial differential equation can then be solved numerically for the resistivity problem.

3.3.1 Finite Difference Equations in Two Dimensions

Finite difference method is used to approximate the solution to the partial differential equation (3.5) using a point-discretization of the subsurface (Mufti, 1976). The computational domain is discretized into $Nx \times Ny$ blocks and the distance between two adjacent points on each block is h in x-direction and l in y-direction, as shown in Figure 3.1.

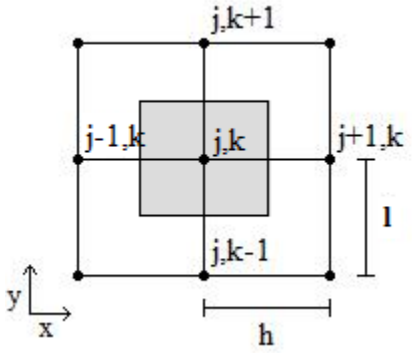

Figure 3.1: Computational domain, discretized into blocks.

Taylor series expansion is used to approximate the derivatives of Equation (3.5) about a point (*j, k*) on the grid,

$$\left.\frac{\partial}{\partial x}\left(\sigma \frac{\partial \phi}{\partial x}\right)\right|_{(j,k)} \approx \frac{\left[\begin{array}{l}\phi(j+1,k)\sigma\left(j+\frac{1}{2},k\right)+\phi(j-1,k)\sigma\left(j-\frac{1}{2},k\right)\\ -\left[\sigma\left(j+\frac{1}{2},k\right)\sigma\left(j-\frac{1}{2},k\right)\right]\phi(j,k)\end{array}\right]}{h^2} \tag{3.6}$$

$$\left.\frac{\partial}{\partial y}\left(\sigma \frac{\partial \phi}{\partial y}\right)\right|_{(j,k)} \approx \frac{\left[\begin{array}{l}\phi(j,k+1)\sigma\left(j,k+\frac{1}{2}\right)+\phi(j,k-1)\sigma\left(j,k-\frac{1}{2}\right)\\ -\left[\sigma\left(j,k+\frac{1}{2}\right)\sigma\left(j,k-\frac{1}{2}\right)\right]\phi(j,k)\end{array}\right]}{l^2} \tag{3.7}$$

The point (*j, k*) represents the shaded area in Figure 3.1 (area = *hl*) so the current density due to an electrode at that point is given by,

$$q(j,k) = \frac{I}{hl} \tag{3.8}$$

where I [amp] is the current injected at point (j, k) Combining Equations (3.5)-(3.8) and solving for the electric potential ϕ at point (j, k) gives,

$$\phi(j,k) = \frac{\left[Ihl + \phi(j+1,k)c_1 l^2 + \phi(j-1,k)c_2 l^2 + \phi(j,k+1)c_3 h^2 + \phi(j,k-1)c_4 h^2\right]}{\left[c_1 + c_2\right]l^2 + \left[c_3 + c_4\right]h^2} \tag{3.9}$$

The parameters c_i represent the conductivity averaged between two adjacent blocks, i.e.

$$c_1 = \frac{2}{\rho(j,k) + \rho(j+1,k)} \tag{3.10}$$

$$c_2 = \frac{2}{\rho(j,k) + \rho(j-1,k)} \tag{3.11}$$

$$c_3 = \frac{2}{\rho(j,k) + \rho(j,k+1)} \tag{3.12}$$

$$c_4 = \frac{2}{\rho(j,k) + \rho(j,k-1)} \tag{3.13}$$

where ρ(j, k) is the resistivity [ohm-m] of the node at grid coordinates j, k.

3.3.2 Iteration method

In order to solve Equation (3.9) numerically and determine the results for electrical potential ϕ at each point on the grid, the iteration method called Successive Over-Relaxation is used (Spencer and Ware, 2009). At first, a guess is made for ϕ(j, k) across the whole grid, for example ϕ(j,k)= for all j,k. That guess is then used to calculate the right hand side of Equation (3.9) for each point and the new set of values for ϕ(j, k) is calculated using the following iteration scheme,

$$\phi_{n+1} = \omega Rhs + (1-\omega)\phi_n \tag{3.14}$$

The multiplier ω is used to shift the eigenvalues so the iteration converges better than simple relaxation. The number ω is between 1 and 2, and when the computing region is rectangular the following equation can be used to get a reasonable good value for ω,

$$\omega = \frac{2}{1+\sqrt{1-R^2}} \tag{3.15}$$

where

$$R = \frac{\left(\cos\left(\frac{\pi}{Nx}\right) + \cos\left(\frac{\pi}{Ny}\right)\right)}{2} \tag{3.16}$$

The natural Neumann boundary condition is used on the outer boundaries in this project, i.e. $\frac{\partial\phi}{\partial n} = 0$.

3.4 RESULTS

The resistivity model is used to calculate the potential difference for a large number of fracture patterns, to investigate whether the results can be used to imply a fracture pattern

for an unknown field. After defining the number of fractures, the model creates horizontal and vertical fractures of random sizes and at random locations. Figure 3.2 shows the results for two different fracture patterns (grey blocks), where the potential difference is calculated between two wells (black blocks) modeled at points (-50,50) and (50,-50). The field is 160×160 m^2 with resistivity as 1 Ωm, and the fractures have resistivity 0.001 Ωm.

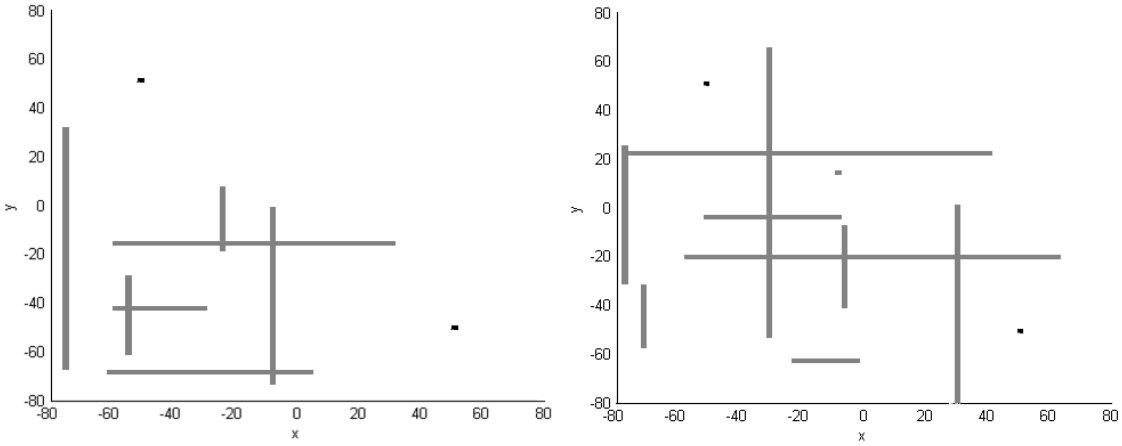

Figure 3.2: Two different fracture patterns modeled (grey blocks).

A current is set equal to 1 A at the well block (black) in the upper left corner of each field, and as -1 A at the well block (black) in the lower right corner, and the potential distribution is calculated. The potential difference between the two wells for the fracture pattern to the left of Figure 3.2 is 2.047 V while the difference is 1.548 V for the pattern to the right. The conductivity of water filled fractures is higher than the conductivity of the rest of the reservoir so higher potential differences between the two wells indicate lower conductivity between them, i.e. fewer fractures. That corresponds to the results for those two fracture patterns; the pattern to the left has higher potential difference and therefore fewer fractures than the one to the right which has lower potential difference. Knowing the potential difference between the wells can therefore help in eliminating a great amount of possible fracture patterns.

Some different fracture patterns give similar potential difference, as the patterns shown in Figure 3.3. The potential difference between the wells is 1.327 V for the fracture pattern to the right and 1.310 V for the pattern to the right. So the difference between the patterns is small even though the patterns are quite different. It is therefore necessary to investigate other ways to facilitate fracture characterization, though the variation in potential distribution for various patterns can be helpful in suggesting some of the fracture properties.

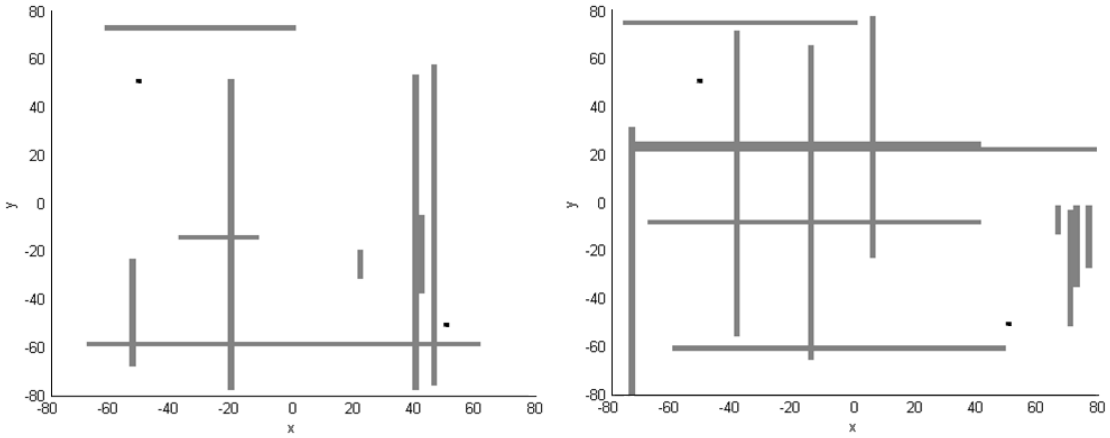

Figure 3.3: Two fracture patterns (grey blocks) that give similar potential difference between two wells (black blocks).

The possibility of using conductive fluid to enhance the contrast between fracture and rock resistivity is explored for the fracture pattern shown in Figure 3.4.

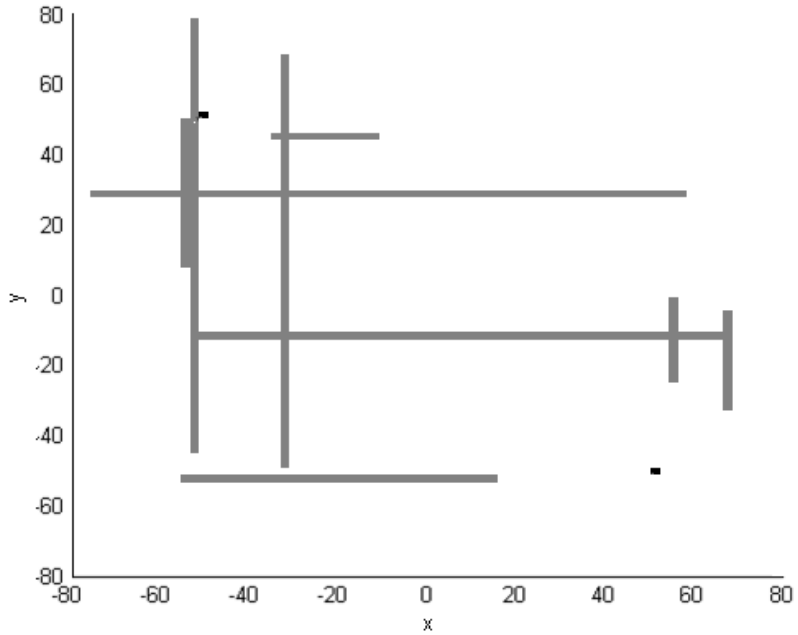

Figure 3.4: A fracture pattern (grey blocks) and two wells (black blocks) used to explore the possibility of using conductive fluid to characterize fractures.

The conductive fluid is assumed to fill up fractures up to a certain x-position and the potential difference is calculated for different positions of the conductive fluid. In Figure 3.5, the potential difference calculated for different x-positions is shown to the left and the change in potential difference within each x-position interval is shown to the right.

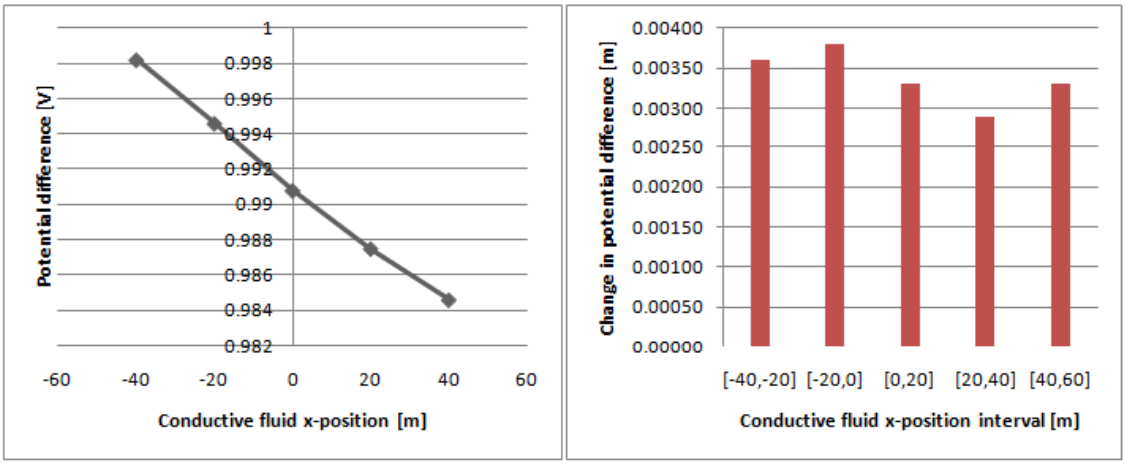

Figure 3.5: Potential difference for fractures filled with conductive fluid up to different x-positions (to the left) and the change in potential difference within each x-position interval (to the right).

As the conductive fluid flows over a larger region, the potential difference between the two wells decreases, because of the increasing conductivity between the wells. The derivative over each interval shows that the smallest change in potential difference is when the conductive fluid extends from -80 m to 20 m up to -80 m to 40 m. The interval from 20 m to 40 m is therefore expected to have the least number of fractures, since filling up the fractures at that interval with conductive fluid does not change much in the potential difference between the well. This holds true in this case since only two horizontal fractures are on that interval as can be seen in Figure 3.4, so getting the potential difference at different time steps when injecting conductive fluid is helpful in getting a better understanding of the fracture properties.

In the results just described, the conductive fluid was assumed to spread uniformly over the whole area, which is obviously not the case when fractures are present. A flow simulation was performed using TOUGH2 reservoir simulator to see how a tracer, which increases the conductivity of the fluid, distributes after being injected into the reservoir. The simulation was carried out on a two-dimensional grid with dimensions $1000\times1000\times10$ m^3. The fracture network can be seen in Figure 3.6, where the green blocks represent the fractures and wells are located at the upper left and lower right corner of the network.

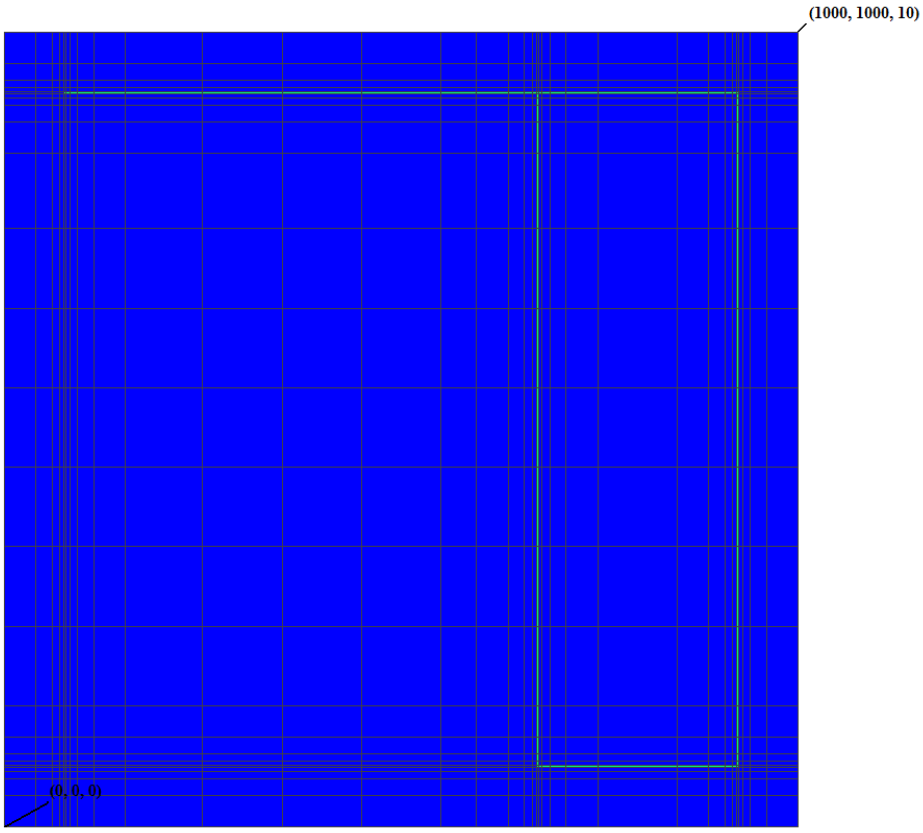

Figure 3.6: Fracture network.

The fracture blocks are given a porosity value of 0.95 and permeability value of 10^{11} md (10^{-4} m^2) and the rest of the blocks are set to porosity 0.1 and permeability 0.1 md (10^{-16} m^2). Closed or no-flow boundary conditions are used and one injector at upper left corner (76, 924) is modeled to inject water at 100 kg/sec with enthalpy 100 kJ/kg, and a tracer at 0.01 kg/s with enthalpy 100 kJ/kg. One production well at lower right corner (924, 76) is configured to deliver heat at 100 J/s.

The initial pressure is set to 1.013 MPa (10.13 bar), temperature to 150°C and initial tracer mass fraction is set to 10^{-9} because the simulator could not solve the problem with zero initial tracer mass fraction. Figure 3.7 illustrates how the tracer transfers through the fractures from the injector to the producer.

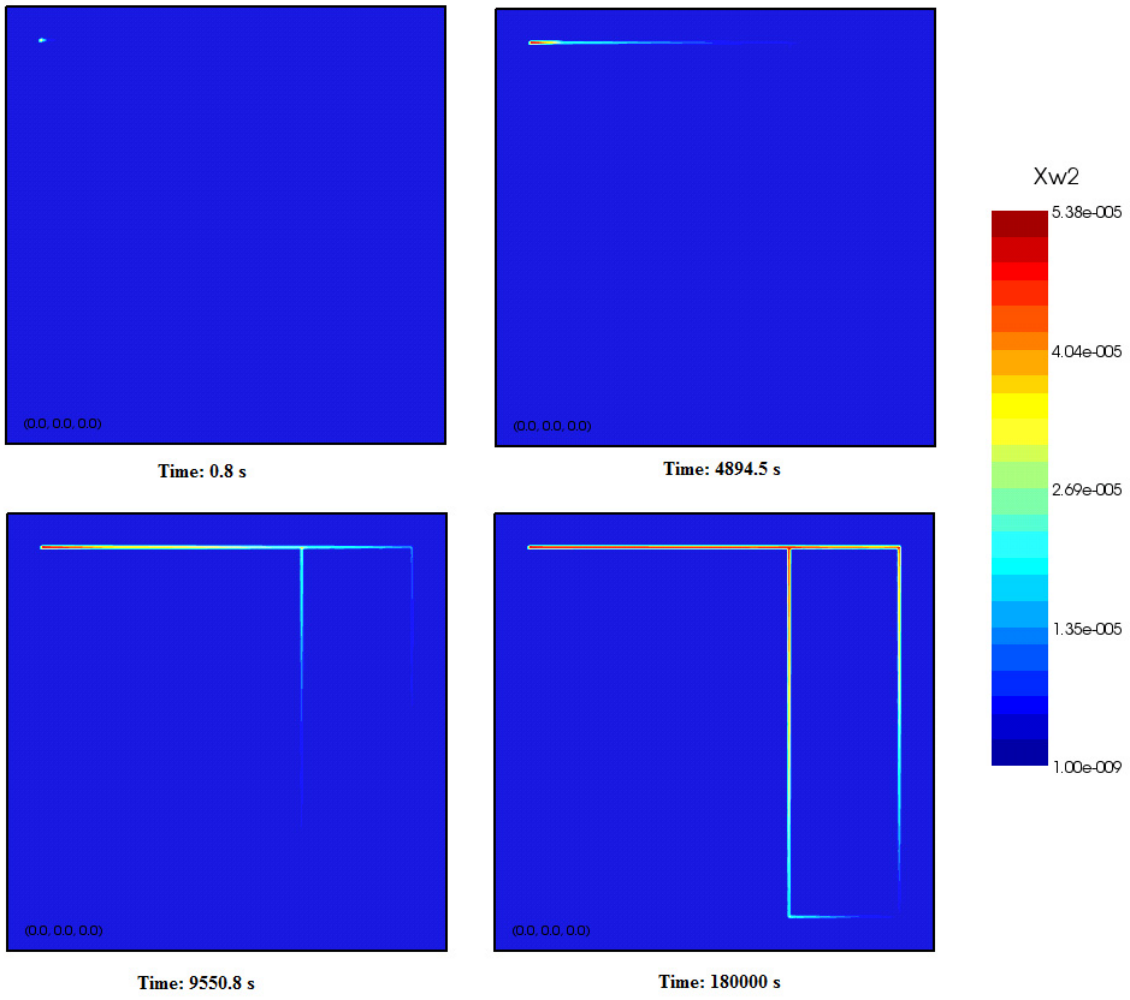

Figure 3.7: Flow simulation, tracer mass fraction.

The tracer flows through the horizontal fracture and starts flowing through the first vertical fracture after approximately 9000 seconds. The tracer has flowed through both the vertical fractures after 180000 seconds and the tracer mass fraction in the fracture network keeps increasing as the production is allowed to continue.

In order to connect the results of the flow simulation to the resistivity model, the grid for the resistivity model needs to be changed. The model is improved so it can solve the potential field for a nonuniform rectangular grid, so the fracture elements can be modeled smaller than the elements for the rest of the reservoir. The total number of elements can thereby be reduced. Figure 3.8 shows the improved grid for the resistivity model, which corresponds to the grid used for the flow simulation.

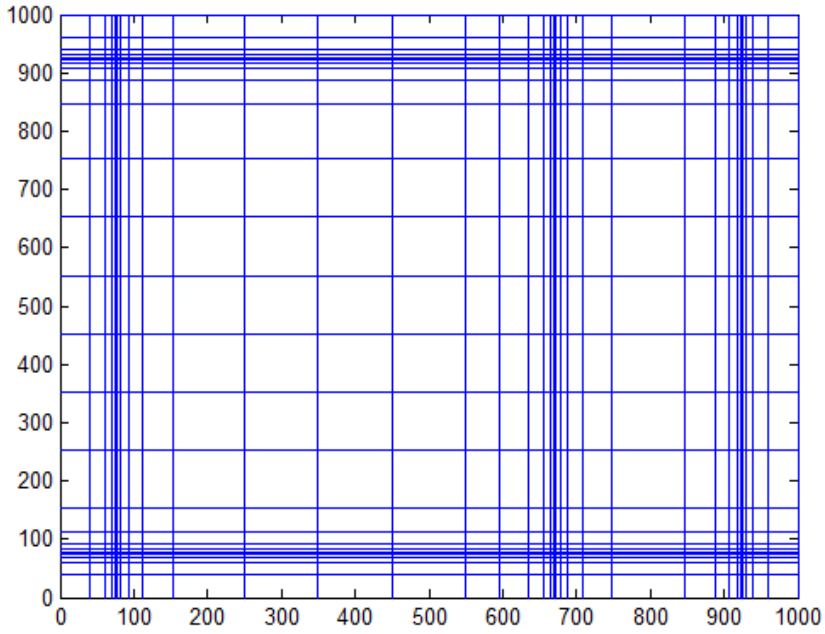

Figure 3.8: Improved grid for the resistivity model.

The grid for the resistivity model is the same as the grid for the flow simulation so the results from the flow simulation can be used directly to assign conductivity values for the potential field calculations.

3.5 FUTURE WORK

One of the next steps is to connect the flow simulator to the resistivity model so that the results from the flow simulation can be read directly and conductivity values assigned for the reservoir. The potential difference will be calculated at different time steps as the tracer flows through the fracture network, and the results studied to infer the fracture properties.

Other future goals are to study the influences of temperatures on water resistivity as well as the potential changes due to fluid stream in the fractures. Also, the effects of mineralization will be examined because it can be difficult to distinguish between rock and fractures containing a lot of minerals.

4. REFERENCES

Amyx, J. W., Bass, D. M. Jr., and Whiting, R. L.: *Petroleum Reservoir Engineering, Physical Properties.* McGraw-Hill Book Co. (1960)

Arnason, K.: Viðnámsmælingar í Jarðhitarannsóknum á Íslandi, Orkustofnun, Orkuþing (2001).

Chen, Hongjie, Li, Zhiwei, Wu, Zhishen and Zhang, Zhijun: "A novel route to prepare and characterize Sn-Bi nanoparticles," *Journal of Alloys and Compounds*. 2005, **394**, 282-285.

Connor, Steve. <stconnor1@gmail.com> (2010, March 11). [Personal email].

Den Iseger, P., Numerical transform inversion using Gaussian quadrature. *Probability in the Engineering and Informational Sciences*, **20(01)**, (2005), 1–44.

Dey, A. and Morrison, H.F.: Resistivity Modelling for Arbitararily Shaped Two-Dimensional Structures, Geophysical Prospecting 27, I06-I36, University of California, Berkeley, CA (1979).

Holder, D.S.: Electrical Impedance Tomography: Methods, History and Applications, IOP, UK (2004).

Horne, R., and Rodriguez, F., Dispersion in tracer flow in fractured geothermal systems, *Proceedings of Seventh Workshop on Geothermal Reservoir Engineering*, Stanford University, Stanford, CA, (1983), 103-107.

Kanj, M., Funk, J., and Al-Yousif, Z.: "Nanofluid Coreflood Experiments in the Arab-D," SPE paper 126161, presented at the 2009 SPE Saudi Arabia Technical Symposium and Exhibition held in Saudi Arabia, Alkhobar, May 09-11.

Lecoanet, H.F., Bottero, Jean-Yves and Wiesner, M.R.: Laboratory Assessment of the Mobility of Nanomaterials in Porous Media. *Environ. Sci. Technol*. 2004, **38**, 5164-5169.

Levitan, M., Deconvolution of multi-well test data. In *SPE Annual Technical Conference and Exhibition,* (2006), 24-27.

Lu, Yu, Yin, Yadong, Mayers, Brian T., and Xia, Younan: "Modifying the Surface Properties of Superparamagnetic Iron Oxide Nanoparticles through a Sol-Gel Approach," *Nano Letters*. 2002, **2**, 182-186.

MathWorks: Partial Differential Equation Toolbox 1, The MathWorks^{TM}, Inc. (2003).

Mufti, I.R.: Finite-Difference Resistivity Modeling for Arbitrarily Shaped Two-Dimensional Structures, *Geophysics*, **41**, (1976), 62-78.

Poulton, S., Raiswell, R.: Chemical and physical characteristics of iron oxides in riverine and glacial meltwater sediments. *Chem. Geol.* 2005, **218**, 203–221.

Schroeter, T. v., and Gringarten, A., Superposition Principle and Reciprocity for Pressure-Rate Deconvolution of Data From Interfering Wells. *SPE Annual Technical Conference*, (2007).

Spencer, R.L. and Ware, M.: Computational Physics 430, Partial Differential Equations, Department of Physics and Astronomy, Brigham Young University (2009).

Stacey, R.W., Li, K. and Horne, R.N.: Electrical Impedance Tomography (EIT) Method for Saturation Determination, *Proceedings*, 31st Workshop on Geothermal Reservoir Engineering, Stanford University, Stanford, CA (2006).

Stehfest, H., Numerical inversion of Laplace transforms. *Communications of the ACM*, **13(1)**, (1970), 47-49.

Tipping, E.,. The adsorption of aquatic humic substances by iron oxides. *Geochim. Cosmochim. Acta* 1981, **45**, 191–199.

Tipping, E., Cooke, D.: The effects of adsorbed humic substances on the surface charge of goethite (a-FeOOH) in reshwaters. *Geochim. Cosmochim. Acta* 1982, **46**, 75– 80.

Wang, P. and Horne, R.N.: Integrating Resistivity Data with Production Data for Improved Reservoir Modelling, SPE 59425, SPE Asia Pacific Conference, Yokohama, Japan (2000).

Watanabe, K., and Takahashi, H., Fractal geometry characterization of geothermal reservoir fracture networks. *Journal of Geophysical Research-Solid Earth*, **100(B1)**, (1995).